



# Cyrene- and water-based exfoliation of black phosphorus for potential nanolayer-mediated disaggregation of insulin fibrils

Carla Caponio<sup>a</sup>, Agata Costanzo<sup>a</sup>, Serena Coiai<sup>a</sup>, Francesca Cicogna<sup>a</sup>, Emanuela Pitzalis<sup>a</sup>, Silvia Borsacchi<sup>a</sup>, Giulia Lorenzetti<sup>a</sup>, Emilia Bramanti<sup>a</sup>, Alessia Papalini<sup>b</sup>, Antonella Battisti<sup>b</sup>, Antonella Sgarbossa<sup>b,\*</sup>, Elisa Passaglia<sup>a,\*</sup>

<sup>a</sup> National Research Council-Institute for the Chemistry of Organometallic Compounds (CNR-ICCOM), SS Pisa, Via Moruzzi 1, 56124 Pisa, Italy

<sup>b</sup> National Research Council-Istituto Nanoscienze (CNR-NANO) and NEST-Scuola Normale Superiore, Piazza S. Silvestro 12, I-56127 Pisa, Italy

## ARTICLE INFO

### Keywords:

Phosphorene  
2D-bP  
Water nanolayers suspensions  
Photoactivity  
Insulin fibrils disaggregation

## ABSTRACT

Liquid suspensions of phosphorene nanolayers (2D-bP) obtained through liquid phase exfoliation (LPE) of elemental black phosphorus (bP) have been prepared and extensively characterized. The exfoliating ability of deionized water (DI water), dihydrolevoglucosenone, (Cyrene), and N-methyl-2-pyrrolidone (NMP) has been investigated and compared along with the differences in the structure, concentration, and stability of the collected nanoflakes. Water was chosen as an exfoliating medium due to its harmlessness and cost-effectiveness and because it is the safest solvent for further potential biomedical applications. Cyrene is a new bio-based solvent still under study. NMP, which is among the most widely used solvents for the exfoliation of 2D systems including bP, has been employed for comparison. The obtained suspensions have been characterized by Dynamic Light Scattering (DLS), Inductively Coupled Plasma Optical Emission Spectrometry (ICP-OES), Phosphorus <sup>31</sup> Nuclear Magnetic Resonance (<sup>31</sup>P NMR), Transmission Electron Microscopy (TEM), Ultraviolet-Visible (UV-Vis), and Raman spectroscopies. The stability of 2D-bP suspensions over time and their photoactivity, i.e., their ability to generate singlet oxygen species as a photosensitizer, have been investigated. The collected results evidenced that the exfoliation of bP in different solvents, including DI water, resulted in satisfactory and comparable nanoflake structures and features. The singlet oxygen generation through irradiation of 2D-bP in DI water suspensions, advantageously obtained directly from LPE, showed promising potential for use in photodynamic therapy (PDT). Preliminary data on the potential biomedical application of 2D-bP to inhibit the insulin self-assembly into amyloid aggregates as well as to cause fibrils disassembling through simple incubation or photoactivity, are also discussed.

## 1. Introduction

The use of phosphorene (2D-bP, nanolayers or nanoflakes obtained by bP exfoliation) has been the research topic of many biomedical investigations [1]. The unique characteristics of 2D-bP, such as its high puckered surface area, ability to adjust its bandgap, high charge mobility, efficient photothermal conversion, and capability to generate singlet oxygen species when exposed to visible NIR radiation, make it an appealing option for developing nanodrugs. These systems can be used to treat various diseases through photothermal (PTT) and photodynamic (PDT) therapy [2–5]. 2D-bP has been investigated for the potential use in neurodegenerative diseases such as Alzheimer's disease (AD) [6,7], triggered by the aberrant self-assembly (misfolding) of the A $\beta$  amyloid

peptide (A $\beta$ ) into fibrillary aggregates [8]. For example, a photosensitizing nanoplateform designed by combining 2D-bP with a thioflavin T derivative, 4-(6-methyl-1,3-benzothiazole-2-yl) phenylamine (BTA), showing high affinity to A $\beta$  peptide, has been NIR irradiated to *in situ* oxidize A $\beta$  peptide, reducing the A $\beta$  plaques-induced cytotoxicity [6]. A $\beta$  inhibitor (LK7) has been coupled with a PEG-stabilized 2D-bP nanoflakes to powerfully inhibit A $\beta$  fibrillogenesis through direct binding and ultimately rescue cells from death [9]. Additionally, 2D-bP can cross the blood-brain barrier (BBB) and are biodegradable *in vivo*. They release nontoxic intermediates like phosphates and phosphonates that can be easily metabolized in the human body. However, the toxicity assessment of 2D-bP, even if claimed [5] is still under investigation, and further advancements are needed for a systematic protocol design

\* Corresponding authors.

E-mail addresses: [antonella.sgarbossa@nano.cnr.it](mailto:antonella.sgarbossa@nano.cnr.it) (A. Sgarbossa), [elisa.passaglia@pi.iccom.cnr.it](mailto:elisa.passaglia@pi.iccom.cnr.it) (E. Passaglia).

<https://doi.org/10.1016/j.flatc.2024.100665>

Received 8 February 2024; Received in revised form 15 April 2024; Accepted 22 April 2024

Available online 24 April 2024

2452-2627/© 2024 The Author(s). Published by Elsevier B.V. This is an open access article under the CC BY license (<http://creativecommons.org/licenses/by/4.0/>).

implementation [10,11]. Interestingly, the potential of 2D-bP in disaggregating protein amyloid fibrils has also recently been tested using model proteins, such as insulin. In this case, black phosphorus quantum dots (BPQDs) have been found to possess the ability to inhibit insulin aggregation and disassemble formed mature fibrils, even at an ultralow concentration (100 ng/mL) [12].

The 2D-bP suitable for biomedicine is commonly obtained by ultrasonic liquid phase exfoliation (LPE). In recent years, organic solvents with different chemical and physical characteristics have been tested to design simple procedures capable of producing nanosheets (nanoflakes) or quantum dots with good yields and reproducible dimensions tuned to the experimental conditions.

Reviews and systematic studies [13–15] have shown that achieving the targets mentioned above requires the use of high-boiling organic solvents, which can be toxic to health and the environment and are not particularly eco-friendly. Among these, dimethyl sulfoxide (DMSO), N-methyl-2-pyrrolidone (NMP), N-cyclohexyl-2-pyrrolidone (CHP) and N,N-dimethylformamide (DMF) are especially effective in producing nanosheets and quantum dots [14–16] having dimensional and photo-physical characteristics suitable for their use in the biomedical field [13].

The exfoliation effectiveness mainly depends on the surface tension of the solvent, which should approach the interlayer energy of the bulk bP to maximize the exfoliation yield and possibly inhibit the re-stacking of the nanosheets [13]. Based on quantum chemical calculations, the exfoliation energy of bP is  $151 \div 92$  meV per atom [17,18], and phosphorene multilayers have a surface energy of about  $59$  mJ/m<sup>2</sup>. In agreement with these data, a solvent surface tension value of about  $40$  mJ/m<sup>2</sup> (which has been predicted as satisfactory for the purpose) is necessary [15,19]. NMP, DMSO and DMF have surface tensions equal to the required value, thus consistent with good exfoliation results [13,14]. However, other physical properties, such as viscosity, density and polarity, poorly considered and discussed in the literature regarding bP exfoliation yields, could influence the stability of the obtained suspensions. These properties can affect nanoflake solvation, inhibiting re-aggregation and preventing reprecipitation phenomena. NMP, DMF, and DMSO have high dielectric constant (ranging from 32.2 to 46.7) and high dipole moment values (being about 4 D), suggesting that these physical features play a role in the exfoliation effectiveness, possibly promoting the formation of a “solvation shell” able to shield and protect 2D-bP from re-aggregation. These solvent molecules surrounding the nanolayers are difficult to remove and they remain even after the necessary steps to collect the products for their ultimate use. To prevent any contamination from toxic solvents, it is recommended to use water or other safe solvents for the LPE of bP. This is especially important for biomedical applications. Instead of using NMP which is commonly utilized, even in Whang et al’s study [12] on insulin fibril disaggregation, it is advisable or rather compulsory to opt for safer alternatives.

Water and Cyrene™ (dihydrolevoglucosenone) have been used in this work as liquid media for the ultrasound-assisted LPE bP exfoliation, carried out in mild conditions. Several LPE runs have also been carried out by using NMP as a reference solvent for comparison purposes.

Water was chosen because harmless and cost-effective and because it is safe for potential biomedical applications. Water-based LPE of bP has been investigated in a few papers [20] reporting not very stimulating results [13,14]. Even though the surface tension is high ( $72$  mJ/m<sup>2</sup>) and the viscosity or density values are similar to those of the performant solvents, the low yields and weak stabilization outcomes can only be improved by adding low- or high-molecular-weight chemicals such as isopropanol [21] sodium dodecyl sulphate [22], and polyvinylpyrrolidone [23]. These chemicals act as stabilizers/surfactants and then remain on the particle surfaces. No systematic study has examined the impact of different operating conditions for the LPE in water alone and aimed to provide convincing results.

Cyrene is considered a safer, bio-degradable solvent [24,25] defined as “practical non-toxic” to the environment according to the Global

Harmonized System of Classification and Labelling of Chemicals (GHS) and readily biodegradable to carbon dioxide and water in 14 days with a biodegradability rate of 99 % [26]. Its use for biomedical applications is under investigation [27] and recently its ability to form poly(lactic-co-glycolic acid) nanoparticles suitable for drug delivery has been assessed [28]. Based on the hen’s egg test, Cyrene has demonstrated biocompatibility with residual content below 2.5 wt%, making it a potential alternative to NMP [28]. Cyrene has never been tested to exfoliate bP, but results achieved for the preparation of graphene and the fabrication of two-dimensional transition metal dichalcogenides-based devices seem promising [29–31].

The 2D-bP prepared in this work by LPE in DI water, Cyrene, and NMP have been characterized by UV-Vis, ICP, DLS, <sup>31</sup>P NMR, TEM and Raman spectroscopies. The results have been discussed concerning the chemo-physical properties of the solvents used. A study of 2D-bP photoactivity has also been performed on suspension obtained through the exfoliation process in DI water, with a particular focus on 2D-bP ability to produce singlet oxygen. Finally, water-based suspensions of 2D-bP have been used without further treatment to test their potential to prevent aggregation and to disaggregate insulin fibrils.

## 2. Materials and methods

### 2.1. Materials

All the solvents and reagents listed below were used as received without further purification if not specified.

Ultrapure water Milli-Q 18.2 MΩ·cm, PureLab Pro, ELGA LabWater, High Wycombe, Bucks, UK; deionized water (DI water) was used throughout and degassed before use. 1-Methyl-2-pyrrolidone C<sub>5</sub>H<sub>9</sub>NO (NMP), ≥ 99.5 % purity, from Sigma Aldrich,  $d = 1.028$  g/cm<sup>3</sup>, Molar Mass = 99.13 g/mol, CAS: 872-50-4; dihydrolevoglucosenone C<sub>6</sub>H<sub>8</sub>O<sub>3</sub> (Cyrene™), ≥ 98.5% purity, from Sigma Aldrich, Molar Mass = 128.13 g/mol,  $d = 1.25$  g/cm<sup>3</sup>, CAS: 53716-82-8; ethanol C<sub>2</sub>H<sub>6</sub>O absolute for analysis, from Supelco-Sigma Aldrich, Molar Mass = 46.07 g/mol, CAS: 64-17-05; 1,3-diphenylisobenzofuran C<sub>20</sub>H<sub>14</sub>O (DPBF), ≥ 96.5 % purity, from Sigma Aldrich, Molar Mass = 270.32 g/mol, CAS: 5471-63-6; thioflavin T C<sub>17</sub>H<sub>19</sub>ClN<sub>2</sub>S (ThT), Molar Mass = 318.87 g/mol, CAS: 2390-54-7; human insulin C<sub>257</sub>H<sub>383</sub>N<sub>65</sub>O<sub>77</sub>S<sub>6</sub>, from Sigma Aldrich, Molar Mass = 5807.57 g/mol, CAS: 11061-68-0.

Preliminary tests of exfoliation (runs reported in the Supporting Information (SI) file) were carried out by using black phosphorus (bP) prepared as previously reported in the literature [32]. Other runs were carried out by using commercial bP (bP, 99.998 % purity) provided by Smart Elements (High pure Black Phosphorus – large crystals SKU: 03933).

### 2.2. Instrumentations

**UV-vis spectroscopy.** UV-Vis absorption spectra were recorded at room temperature with a Jasco V-750 UV-visible spectrophotometer. Spectra were recorded at room temperature in the 200–900 nm region. The liquid sample was analysed using quartz cuvettes.

**NMR spectroscopy.** <sup>31</sup>P NMR spectrum of 2D-bP in water was recorded with a Direct Excitation (DE) experiment, under Magic Angle Spinning (MAS) conditions (spinning rate 10 kHz) and High-Power Decoupling from <sup>1</sup>H nuclei. The experiment was run on a Bruker Avance Neo spectrometer working at <sup>1</sup>H and <sup>31</sup>P Larmor frequencies of 500.13 MHz and 202.46 MHz, respectively, equipped with a double channel probe head, accommodating rotors with an outer diameter of 4 mm. In order to obtain a quantitative spectrum a recycle delay between two consecutive scans of 90 s was used, which is more than 5 times the <sup>31</sup>P T<sub>1</sub> of 2D-bP in a solvent, i.e., 16 s [33] and 2832 scans were accumulated.

**Dynamic Light Scattering.** DLS measurements were performed with a NanoZetaSizer apparatus model ZEN1600 (Malvern, Worcestershire, UK) equipped with a HeNe laser (633 nm, 4 mW) and an avalanche

photodiode detector with an angle of  $173^\circ$ . The hydrodynamic diameter values were extracted from cumulant analysis and multimodal size distribution algorithm non-negative least square (NNLS). For each measurement, autocorrelation functions were averaged and evaluated by the Dispersion Technology Software (DTS) (Malvern Instruments Ltd., Malvern, UK). The liquid sample was analysed in a glass cuvette.

**Inductively Coupled Plasma Optical Emission Spectroscopy.** ICP-OES was used to evaluate the amount of elemental P in the 2D-bP suspensions. Three different samples of 2D-bP (450  $\mu\text{L}$ ) each obtained from DI water, Cyrene, and NMP solvent, were dissolved in 2 mL of  $\text{HNO}_3$  (Fluka, TraceSELECT™ for trace analysis > 69 %) and 1 mL of  $\text{H}_2\text{O}_2$  30 % (Sigma Aldrich, >30 % for trace analysis) and heated for 2 h at boiling temperature to digest the organic part. The mixture was then diluted to 25 mL with ultrapure water for ICP-OES analysis. Phosphorus determination was carried out with an Optima 8000 ICP-OES (Perkin Elmer, Waltham, MA, USA) operating at 1500 W and equipped with an auto-sampler S10, MiraMist® Nebulizer and cyclonic chamber. Argon (420.069 nm) was used as internal standard. Calibration solutions were obtained by dilution of commercial standard solutions (Fluka TraceCERT®) in  $\text{HNO}_3$  2 %. The phosphorus emission signal was measured at 213.617 nm.

**Raman spectroscopy.** Raman spectroscopy was performed using an inVia instrument (Renishaw, Wotton-Under-Edge, UK) coupled with an optical Leica DLML microscope (Leica Microsystems, Wetzlar, Germany), equipped with an NPLAN 50 $\times$  objective (spot size of about 5  $\mu\text{m}$  in diameter). The instrument has a He-Ne and diode laser source at  $\lambda = 633$  nm ( $P_{100\%} = 11.15$  mW) and  $\lambda = 785$  nm ( $P_{100\%} = 78.20$  mW) wavelength, respectively. The spectral calibration of the instrument was performed on the  $520.5\text{ cm}^{-1}$  band of a silicon wafer. The spectral resolution was  $0.5\text{ cm}^{-1}$ , and the spectral range was between 100 and  $1200\text{ cm}^{-1}$ . The power used (0.5, 1 or 5 %) was calibrated according to the sample under investigation, avoiding signal saturation on the CCD detector, while the acquisition time was 10' and the number of accumulations equal to 5. The samples of 2D-bP suspension were analysed in the form of films obtained by dropping them onto a glass slide and dried in a vacuum oven at  $40^\circ\text{C}$  for 45 min.

**Fluorescence spectroscopy.** Fluorescence measurements were performed with a Horiba instrument FluoroMax4-TCSPC. The liquid sample was analysed in a high-precision quartz cuvette. The emission spectra were recorded using a  $\lambda_{\text{exc}} = 442$  nm (see Methods). The data were processed using FluorEssence data management software (Origin8).

**Infrared spectroscopy total reflectance mode.** A FT-IR Perkin-Elmer Frontier spectrometer equipped with an ATR accessory with a diamond crystal was used for the analysis. Spectra were recorded at room temperature in the  $4000\text{--}600\text{ cm}^{-1}$  region. For each sample, 32 interferograms were recorded, averaged, and Fourier-transformed to produce a spectrum with a nominal resolution of  $4\text{ cm}^{-1}$ . Thirty-two scans were enough to obtain a suitable S/N ratio and to keep a balance of aqueous vapor bands with respect to the background spectrum. Perkin-Elmer software and an in-house LabVIEW program for peak fitting were employed to run and process spectra, respectively. The LabVIEW program for peak fitting was previously described based on previous works [34,35]. The choice of the amide I band for structural analysis is due to the very low contribution of the amino acid side chain absorptions present in this region [36], and to its higher intensity with respect to other amide modes. One to two microliters of the samples of insulin fibrils incubated or not with 2D-bP were cast on the ATR diamond and the solvent was allowed to evaporate before recording the spectrum.

**Confocal Microscopy.** Confocal fluorescence imaging was performed using a Leica TCS SP5 inverted confocal microscope (Leica Microsystems AG, Wetzlar, Germany) equipped with an external pulsed diode laser for excitation at 405 nm. The detection range was set between 450 and 550 nm. The laser repetition rate was set to 40 Hz. The image size was  $512 \times 512$  pixels and the scan speed was set to 400 Hz (lines per second). The objective was a HCX PL APO CS 63.0  $\times$  1.20 NA water immersion objective (Leica Microsystems) and the pinhole aperture was set to 0.5

Airy (78  $\mu\text{m}$  confocal aperture).

**Transmission Electron Microscopy.** TEM analysis was conducted using an HR-TEM 200 kV ZEISS LIBRA 200 FE (Carl Zeiss AG, Jena, Germany) equipped with a second-generation in-column  $\Omega$  filter, and HAADF detector. The 2D-bP suspension in  $\text{H}_2\text{O}$  obtained after centrifugation at 7000 rpm was centrifuged at 14000 rpm, removing the supernatant and drying the precipitated flakes in a vacuum oven at  $40^\circ\text{C}$  for 30 min. Samples were then dispersed in ethanol, stirred, and deposited on the instrument support, letting the solvent evaporate.

### 2.3. Methods

**2D-bP suspensions** were prepared by ultrasound-assisted LPE of bP using previously degassed DI water, Cyrene or NMP as solvents and variable black phosphorus concentration (for standardized experiments about 1 mg/mL). Briefly, 4 mL of solvents and 4 mg of bP were introduced into 10 mL Schlenk under an inert atmosphere performed after 3 nitrogen-vacuum cycles. The suspension was subjected to a continuous sonication process using a Hielscher Ultrasonic Processor UP200St (200 W, 26 kHz, Seneco Science) equipped with the Sonotrode S26d2 probe (diameter of the tip 2 mm) at the 50 % amplitude setting, generating 5 W power (with about 5 mm immersion depth) in an inert atmosphere (flow nitrogen) for 5 h. During sonication, the Schlenk was immersed in a bath of water and ice to prevent heating of the suspension. The obtained dispersion, of a dark grey colour, was centrifuged for 15 min at 7000 rpm to remove the un-exfoliated parts, using an Eppendorf centrifuge model 5804R. The as-obtained suspension was used for further analysis.

**Irradiation experiments** were conducted by adding 1 mL of a 50:50 ethanol: water DPBF solution to 1 mL of 2D-bP suspension. The concentrations of DPBF and 2D-bP are always in a ratio of 2:1. As a light source, the Xenon lamp of the FluoroMax-4 was used. The irradiation experiments were performed recording an excitation spectrum in the 650–1150 nm range with a 20 nm slit. The  $^1\text{O}_2$  production was then confirmed by UV-vis measurements.

The measurements under an oxygenated environment were performed after 10 min oxygen bubbling in the cuvette.

**Preparation of insulin fibrils with and without 2D-bP.** Human insulin was dissolved in 20 % v/v glacial acetic acid (pH 2.5) and 25 mM sodium chloride (NaCl) and incubated at  $60^\circ\text{C}$  in a thermomixer with mechanical shaking at 600 rpm to induce fibril formation up to 3 days with or without 2D-bP (0.001 mg/mL). NaCl allowed the formation of fibrils after shorter incubation time. The final concentrations of insulin fibrils and 2D-bP were 2.5 mg/mL and 2.5  $\mu\text{g}/\text{mL}$ , respectively.

**Thioflavin T spectrofluorometric measurements on insulin.** 10  $\mu\text{L}$  of insulin sample at different times of fibrillogenesis with or without 2D-bP were diluted in 600  $\mu\text{L}$  of 25  $\mu\text{M}$  aqueous ThT solution. After static staining, the fluorescence intensity of ThT was measured at  $\lambda_{\text{ex}} = 442$  nm in a 1 cm quartz cuvette with both excitation and emission slit widths at 5 nm. The fluorescence signal was recorded in the 450–700 nm range, and the emission at 480 nm was used to monitor the kinetics of insulin fibrillation.

**Preparation of insulin fibrils and disaggregation tests induced by irradiation experiments.** Mature fibrils were prepared as described above. Three samples were then prepared: Sample A containing 130  $\mu\text{L}$  of fibrils solution (2.5 mg/mL insulin concentration) and 1 mL of 2D-bP DI water suspension (6.7 mg/L); Sample B: 130  $\mu\text{L}$  of fibrils solution and 1 mL of DI water (blank). After 24 h incubation time, sample A was split into two aliquots: A1 was kept into the dark and A2 was irradiated in the conditions used for tracking the singlet oxygen generation by 2D-bP. All the samples were stained by ThT and ThT fluorescence signal measured as reported above (each measurement was carried out by using 600  $\mu\text{L}$  of 25  $\mu\text{M}$  aqueous ThT solution and 25  $\mu\text{L}$  of samples B, A1 and A2).

**Confocal Microscopy.** Confocal fluorescence images of insulin aggregates were taken from samples collected at different times during the aggregation experiments. Samples were stained with ThT as for spectroscopic analyses, then 50  $\mu\text{L}$  aliquots were placed on glass-bottom

dishes, left to settle for two minutes to allow decantation and imaged.

### 3. Results and discussion

#### 3.1. Determination of concentration and size of 2D-bP

The preparation of 2D-bP envisaged the LPE assisted by ultrasound, using a sonotrode tool. The effectiveness of NMP, Cyrene, and DI water in exfoliating bP was investigated. The main chemical-physical features of each solvent are listed in Table 1.

Considering that high powers can cause unwanted breakage of the P-P bonds [20] we preferred to use mild experimental conditions, i.e., using  $P_s = 5$  W of the ultrasound generator by maintaining 50 % of the oscillation amplitude. The sonication time ( $t_s$ ) and initial bP ( $C_i$ ) concentration were set based on preliminary results, which are reported and discussed in the SI (see text, Fig. S1 and Table S1). During the sonication, the cavitation-induced micro bubbling led to an increasingly darker colour with the sonication time. After the sonication process, the suspensions were centrifuged at 7000 rpm for 15 min to distinguish the exfoliated flakes from the bulk bP. The resulting colour provides a rough indication of the 2D-bP concentration, which is higher in the case of NMP (Fig. 1A). Final suspensions were analysed by DLS (Fig. 1B) and UV-Vis spectroscopy (Fig. 1C and D).

DLS measurements were used to determine the size of nanoflakes. This technique provides the average hydrodynamic diameter distribution by modelling the analyzed systems as a set of spherical particles. However, in the case of 2D-bP, which are not spherical but layered sheets/flakes, we assumed that the particle size determined by DLS refers to the diameter of a sphere having the same translational diffusion coefficient as the real 2D-bP. This approach neglects factors like solvent molecule absorptions, nanolayer aggregation phenomena, particle orientation and shape effects, which could impact Brownian motion. Therefore, the numerical data reported in Table 1 reflect the average largest dimension of 2D-bP counted over the total number of particles resulting from a numerical average of the size distributions. DLS analysis shows that depending on the solvent used, the fractionated suspensions (7000 rpm) contained 2D-bP with different sizes moving from about 60 nm for the DI water to 140 nm for Cyrene. Moreover, we observed a decrease in size distribution peaks, which were remarkably narrower for

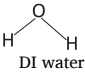

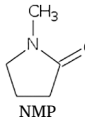
smaller particles (Fig. 1B). The size of particles obtained through the exfoliation procedure depends on the liquid medium's solvation capacity, which also determines the exfoliation yield (discussed below). Furthermore, the dimensions are influenced by the density and viscosity of the solvent. When all suspensions were fractionated at 7000 rpm, the experimental conditions remained constant. The higher the density and viscosity of the solvent, the better its ability to keep larger particles in suspension when subjected to the same centrifugal force. From the comparison of the physical parameters reported in Table 1, it is evident that NMP and Cyrene have densities and, above all, viscosities greater than DI water, and Cyrene is an extremely viscous solvent. The numerical particle size data obtained from LPE in the three solvents correlates with density and viscosity values, exhibiting the following trend: particle diameter (d) in Cyrene > in NMP > in DI water (Table 1 and Fig. 1A). Furthermore, as the average particle diameter increases, we observed a broadening of their distribution since the number of particles with the same or larger diameter increases (Fig. 1B).

Due to the tunable number-of-layer-dependent bandgap, 2D-bP suspensions show a broad absorption spectrum in the entire UV-Vis region regardless of the solvent in which they have been exfoliated. Fig. 1C shows the UV-Vis spectrum in the 350–900 nm region of 2D-bP suspensions obtained by exfoliation in DI water, Cyrene and NMP after centrifugation at 7000 rpm. An absorbance cutoff wavelength is necessary owing to both Cyrene and NMP absorptions below 350 nm. The inset of Fig. 1C shows the full UV-Vis spectrum of 2D-bP produced in DI water showing two characteristic regions of absorption, i.e., a peak at about  $\lambda = 260$  nm and a shoulder in the visible region at about  $\lambda = 466$  nm. This last absorption is common also to the spectra of 2D-bP suspensions obtained in the other solvents [38].

Despite many UV-Vis absorption spectra of 2D-bP suspensions reported in the literature in several solvents [14,22,39], the interpretation of the experimentally observed absorptions remains challenging. This difficulty arises from the highly anisotropic and dichroic nature of phosphorene. Considering the presence of zigzag and armchair crystallographic directions, light is absorbed in different amounts depending on its polarization. It has been calculated [40] that the optical transition from the valence band (VB) to the conduction band (CB) for the bilayer 2D-bP occurs at about 0.72 eV along the armchair direction, while it is 0 between 0 and 2.5 eV along the zigzag direction (which is the tunable

**Table 1**

Chemical structure, density ( $\rho$ ), viscosity ( $\mu$ ), surface tension ( $\gamma$ ), Hansen solubility parameters (dispersive ( $\delta_D$ ), polar ( $\delta_P$ ) and hydrogen bonding ( $\delta_H$ ), respectively) of NMP, Cyrene and DI water\* used for the exfoliation<sup>1</sup>; final concentration of 2D-bP ( $C_f$ )<sup>2</sup>, bP exfoliation yields (wt. %)<sup>2</sup> and 2D-bP size as determined by DLS.

Solvent	$\rho$ at 20 °C (g/mL)	$\mu$ at 25 °C (cP)	$\gamma$ at 20 °C (mJ/m <sup>2</sup> )	$\delta_D$ (MPa) <sup>0.5</sup>	$\delta_P$ (MPa) <sup>0.5</sup>	$\delta_H$ (MPa) <sup>0.5</sup>	$C_f^2$ (mg/L)	Yield <sup>2</sup> (wt. %)	$d^3$ (nm)
 DI water	1.0	1.0	77.2	15.6	16.0	42.3	11 ± 0.51	1.1	63 ± 21
 Cyrene	1.25	14.5	72.5	18.8	10.6	6.9	16 ± 2.0	1.6	142 ± 11
 NMP	1.03	1.65	40.8	18	12.3	7.2	30 ± 4.3	~3	108 ± 7

\* Data were achieved from [27,37] and from:

<https://www.sigmaaldrich.com/deepweb/assets/sigmaaldrich/marketing/global/documents/238/211/greener-solvents-br-mk.pdf>;

<https://www.dataphysics-instruments.com/Downloads/Surface-Tensions-Energies.pdf>;

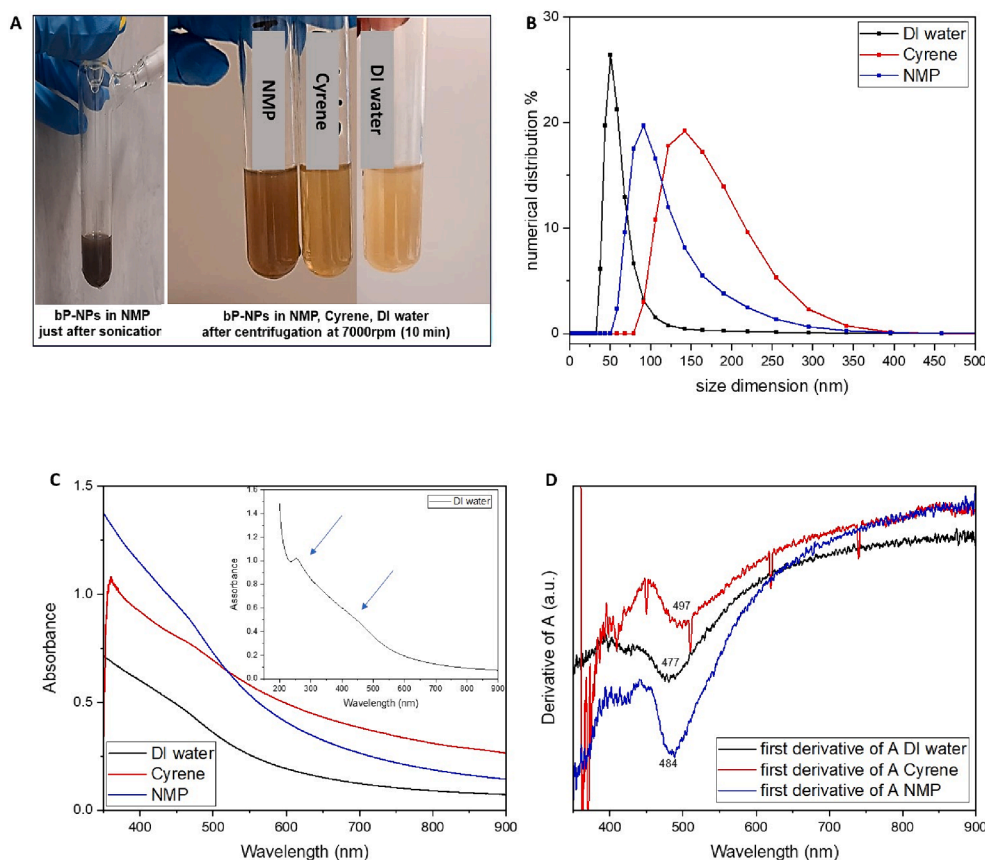
[https://www.accudynetest.com/solubility\\_table.html](https://www.accudynetest.com/solubility_table.html).

<sup>1</sup> $P_s = 10$  w;  $t_s = 4$  h;  $C_i = 1$  mg/mL; suspension obtained after centrifugation at 7000 rpm for 15 min.

<sup>2</sup> $C_f$  and yield % wt values were determined by using UV-Vis measurements by collecting the corrected absorbance data at 466 nm ( $A_{466}$ ). The values of extinction coefficient ( $\epsilon$ ) (L/g cm) necessary to apply the Lambert-Beer law [ $(\epsilon_{NMP}) = 24$  L/g cm;  $(\epsilon_{Cyrene}) = 38$  L/g cm;  $(\epsilon_{DIwater}) = 26$  L/g cm] were determined by measuring the P concentration ( $C_i$ ) by ICP-OES analysis of suspensions obtained by using  $C_i \sim 2$ –3 mg/mL. Exfoliation runs were performed in triplicate for Cyrene and NMP and repeated 5 times for DI water. The data were collected on suspensions centrifugated at 7000 rpm for 15 min.

<sup>3</sup>2D-bP size dimensions as determined by DLS.





**Fig. 1.** A: 2D-bP suspensions in NMP before (right) and in NMP, Cyrene and DI water after (left) centrifugation at 7000 rpm for 15 min; B: Size dimension numerical distribution vs size dimension for 2D-bP obtained by exfoliation in DI water, Cyrene and NMP after centrifugation at 7000 rpm; C: UV-Vis spectra of 2D-bP suspensions obtained by exfoliation in DI water, Cyrene and NMP after centrifugation at 7000 rpm (inset: full spectrum of 2D-bP DI water suspension); D: derivative of spectra reported in C.

band gap interval). Moreover, the calculated optical absorbance revealed a strong absorption along both directions between 4 and 6 eV (which corresponds to the UV-blue wavelength region ranging from 206 to 309 nm). This transition has been related to a more complex photon-induced absorption of electrons between the valence and conduction bands (a secondary high-energy interband transition) [40]. Woomer *et al.* [39] performed the first UV-Vis experimental analysis on bulk bP and phosphorene suspensions, confirming that both systems show identical absorption thresholds, i.e., a low energy and a high energy transition. According to the authors, the low energy transition is related to the band gap since it corresponds to the transition between the highest occupied molecular orbital of the VB and the lowest empty molecular orbital of the CB and it depends on the number of layers (below 1.95 eV or 635.8 nm, i.e., in the visible red region). The high-energy transition corresponds instead to a change between either the next highest occupied band (VB - 1) and the CB, or the VB and the next lowest empty band (CB + 1), even if the former seems to fit better with the numerical energy data [39]. The orbitals involved are supposedly the lone pair's 3p orbitals (py, pz) of the 3p (pz) antibonding orbital. This high energy transition was numerically determined by Tauc analysis and in this case, it was found it depends on the number of the layers ranging from 1.95 eV (635.8 nm) in bulk bP to 3.15 eV (393.6 nm) in a suspension containing primarily monolayers, the thinnest fraction the authors claim to analyse.

In our experiment, UV-Vis spectra were collected directly on the suspensions achieved after centrifugation. Therefore, due to the complexity of the system, which is a suspension of 2D-bP that can move randomly according to Brownian motion, and considering the absorption of non-polarized radiation, the overall absorption is an "average" of

the contributions of all the nanoflakes that make up the sample. In particular, the shoulder of the very broad absorption, which significantly increases in all solvents in the blue range, arbitrarily centred at about 466 nm, is probably due to high-energy transitions of 2D-bP with different numbers of layers. This band, in agreement with the available literature reporting similar spectra [41] was chosen as the reference signal to calculate 2D-bP concentration (Table 1). However, the first derivative of the spectra clearly shows that this shoulder shifts to different wavelengths depending on the nanoparticle suspension species (higher for 2D-bP having larger size dimensions, Fig. 1D), following the earlier discussion on the inhomogeneity of the photophysical properties of the analysed samples.

In all the recorded spectra, we observed a significant drift of the baseline (Fig. 1C), according to the spectra reported in the literature. This effect can be attributed to both the wide-range absorption of 2D-bP from UV to NIR wavelengths and reasonably also to a scattering effect. Although it has been demonstrated [39] that the scattering does not substantially affect the values of the absorption coefficients, at least for nanosheets composed of a low number of layers of unknown size [39], we observed a clear trend of increasing baseline with particle size (Fig. 1C and B). Based on this observation and considering that the size dimension of our 2D-bP ranging from 60 to 140 nm may give scattering effects, we must assume that the collected spectra are probably the sum of the absorption and diffusion of light by the NPs, therefore they are extinction spectra.

Both Rayleigh's and Mie's theories base their hypotheses on spherical models and require knowledge of physical parameters such as the refractive index which, in the case of 2D-bP, can also depend on the number of layers or the degree of exfoliation [42]. Since no type of

absorption at 900 nm is reported for 2D-bP, we decided to subtract the absorbance at 900 nm, which increases with increasing particle size, from the absorbance values at 466 nm, and these “corrected values” were used to calculate the concentration of 2D-bP in the suspensions, using the Lambert-Beer law (Table 1). ICP-OES results were employed to validate the UV-Vis method by correlating the  $A_{466}$ - $A_{900}$  values with the concentration of P. This allowed us to calculate the extinction coefficients of 2D-bP and, thus, to have a method for the determination of the concentration of 2D-bP in all suspensions (see footnotes of Table 1 and Experimental part).

### 3.2. Exfoliation yields

Data reported in Table 1 show that the exfoliation yields are not high even in NMP, the solvent used in this work as a reference, compared to other results reported in the literature [13,14]. It is worth noting that the experimental conditions for LPE, including the power used, were chosen to avoid breaking and minimize oxidation as they can impact the stability of nanosheets, especially in water. However, this approach may have led to a lower yield. Despite the final concentration of nanosheets being low in all solvents, the yield in Cyrene and DI water was approximately one-half and one-third of the yield in NMP, respectively. Surface tension values ( $\gamma$ ) play an important role: 2D materials with high surface energy have high exfoliation efficiency when combined with solvents with suitable surface tension values [43,44]. Upon examining the exfoliation process [13,45] and the crucial role of the surface tension of the liquid medium, it results that the surface tension must have a minimum value higher than the cohesive forces of the 2D system to ensure effective exfoliation. Several studies have attempted to establish a correlation between bP's surface energy and the solvent's surface tension during the LPE process. Despite these studies have not always reported consistent data, most agree that the optimal surface tension range is around 40 mJ/m<sup>2</sup> [43,44,46]. Bonaccorso *et al.* [46] showed that the solvents able to exfoliate bulk bP have a  $\gamma$  value in the range of 25–40 mJ/m<sup>2</sup> estimating the bP surface energy between 50 and 65 mJ/m<sup>2</sup> [13,21,46]. This value matches the surface tension of NMP [13,21,46], while Cyrene and water  $\gamma$  data largely exceed this optimized value [13,45]. Additionally, the matching of surface tension has a significant impact on the stabilization of suspensions. Indeed, even the wettability of the layers affects the final yield; both polar and dispersive energy help to drive the surface interactions between layers and solvents, helping to overcome the interlayer vdW cohesive forces. When both are effective, the solvent molecules can enter the layer space and exfoliate the bulk bP, leading to the stabilization of the exfoliated layers [13,43]. The polarity of the medium is thus influential. The Hansen Solubility Parameters (HSP) were used to correlate the final 2D-bP concentration to the polarity of the solvent because, according to the thermodynamics of the solution, 2D materials mixed with target liquids can be considered as solutions. The HSP parameters reported in Table 1 describe how 2D-bP and the solvent interact, where  $\delta_D$ ,  $\delta_P$  and  $\delta_H$ , represent the dispersion forces, polar, and hydrogen-bonding solubility parameters, respectively [13]. The Hansen parameter's  $\delta_D$ ,  $\delta_P$  and  $\delta_H$  estimated for bP, are in the ranges 15–18, 5–12, 5–10 MPa<sup>0.5</sup> [46], respectively, among which NMP and Cyrene show a better correspondence, as highlighted by the experimental results. DI water fails to reach the values of both polar and hydrogen-bonding parameters (having higher values than the targeted ones), reflecting the polar and protic nature that renders it poorly compatible with 2D-bP, with possibly consequent inefficiency to stabilize the nanosheets during the LPE process. In simpler terms, due to its surface tension, water can break apart the bP and exfoliate the layers (as demonstrated by smaller particle size) but, due to its polar and protic nature, it cannot keep the resulting nanoflakes stable as it does not have the optimal solvation capacity, thus resulting in lower yield and worse stability, as discussed later.

It is also important to examine density and viscosity parameters reported in Table 1, since these factors influence the exfoliation process as

demonstrated by an increase in yield and particle size when either is elevated. In fact, sedimentation effects are remarkably inhibited in Cyrene, resulting in the formation of 2D-bP of larger dimensions and higher concentrations.

Therefore, surface tension and polarity of the solvent are significant factors in the exfoliation process, favoring NMP and Cyrene. Additionally, physical characteristics such as density and viscosity seem crucial for stabilizing nanoflakes over time.

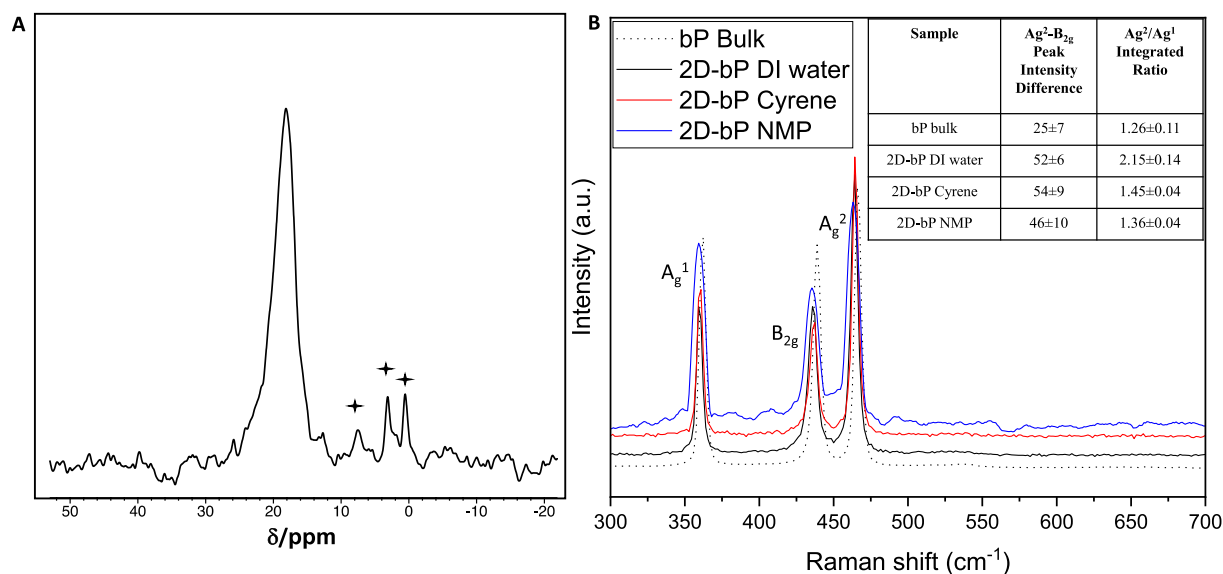
### 3.3. Structural characterizations of 2D-bP

The LPE of bP in an aqueous environment features several issues owing to the possible impairment of the chemical integrity of the exfoliated flakes by oxidation [47–50]. The 2D-bP lone pairs have affinity for oxygen, which can easily interact with the free electron doublets, ultimately leading to the oxidative degradation of the layer. Since oxygen has a high solubility in water (8 mg/L at 25 °C) [51], an initial degradation could happen during the exfoliation when P-P secondary bonds between layers constituting bulk bP are broken to form single and few-layer flakes. Moreover, these flakes present a larger available surface area, which increases the exposure of dangling bonds to the possible interaction with oxygen molecules, thus enhancing the probability and speed of degradation.

The structural integrity, stability and crystallinity of 2D-bP can be evaluated by <sup>31</sup>P NMR and Raman spectroscopies.

<sup>31</sup>P NMR spectroscopy can be used to assess the possible presence of phosphorus species other than bP, generated by oxidation and not detectable by the UV and Raman spectroscopies (discussed below). <sup>31</sup>P NMR was conducted on the whole exfoliated fraction before centrifugation aiming to collect all the P species (Fig. 2A). The spectrum of the 2D-bP suspension in DI water collected after 3 days from its preparation shows the most intense signal at a chemical shift of 18.2 ppm which can be straightforwardly ascribed to 2D-bP, while minor peaks at 0.5, 3.1 and 7.5 ppm are due to species originating from the oxidative degradation of 2D-bP (mainly phosphates and phosphites) [33,52]. By integrating the signals, it is possible to assess that oxidized species account for less than 15 ± 1 % of the total phosphorus content. Considering that it was not possible to establish the possible degree of oxidation of the starting bP, this result confirms that our procedure successfully preserved the bP structure for the majority of nanoflakes exfoliated in DI water.

The Raman spectra of bP consist of three main peaks, one out-of-plane mode ( $A_g^1$  located at 360.8 cm<sup>-1</sup>) and two in-plane modes ( $A_g^2$  and  $B_{2g}$ , located at 465.9 cm<sup>-1</sup> and 437.4 cm<sup>-1</sup> respectively, Fig. 2B) [53]. The positions and the intensity ratios between these peaks change depending on defects and the number of layers [54,55]. Generally, exfoliation promotes a shift to higher wavenumbers, particularly for the  $A_g^2$  mode owing to changes in energetic vibration. By reducing the number of layers in a bP flake, the steric hindrance caused by interactions between the layers is reduced, leading to an increase in vibrational freedom along the bP stacking direction. This generates an increase in the vibrational energy of P to oscillate within the layer and consequently a blue Raman shift [38]. Despite these considerations, it is not trivial to define a relationship between the vibrational frequencies and the number of layers. An appreciable shift towards higher energies is observed only for the  $A_g^2$ ; anyway, since the variations (2–3 cm<sup>-1</sup>) reported in the literature (both in theoretical [56] and experimental [38] studies) fall into instrumental error, they are therefore not completely reliable [57]. An effective blue shift of the  $A_g^2$  peak is experimentally evident only for monolayer and bilayer bP, while it is irrelevant as the number of layers increases [57]. In our case, it was not possible to evidence significant differences between the shifts of the resonance peaks of 2D-bP and those of bulk bP (Fig. 2B) as the flakes have likely more than 2 layers [15]. The slight enlargement of peaks may be related to a decrease in crystallinity. Some insight into flakes' thickness can be gained by analysing the intensity differences of  $A_g^2$  and  $B_{2g}$  peaks and the



**Fig. 2.** A:  $^{31}\text{P}$  DE-MAS NMR spectrum of 2D-bP exfoliated in DI water (before centrifugation). B: Raman spectra of bulk bP and 2D-bP exfoliated in DI water, Cyrene and NMP. Inset: intensity differences of  $\text{Ag}^2$  and  $\text{B}_{2g}$  peaks, and integrated ratio of  $\text{Ag}^2$  to  $\text{Ag}^1$ ; the spectra were obtained from five different points of the same sample. The numerical data's relative standard deviation is provided in the inset Table.

integrated peak area ratio of  $\text{A}_g^2$  to  $\text{A}_g^1$  (both increasing by reducing the number of layers) [57,58]. From our measurements (inset in the Fig. 2B), we observed that the difference between  $\text{A}_g^2$  and  $\text{B}_{2g}$  peak intensity is 25 for bulk bP, whereas it ranges between 46 and 54 for 2D-bP [58] suggesting that the signal of 2D-bP derives from few-layer flakes structures possibly with lower layer numbers for the samples exfoliated in DI water. Concerning the integrated ratio of  $\text{A}_g^2$  to  $\text{A}_g^1$  peaks, we found that it is 1.26 for bulk bP and it is higher for the exfoliated flakes in agreement with the values reported in the literature [58] (once again higher for DI water-sonicated sample), according to which the ratio between the integrated areas of the peaks increases as the number of layers decreases. This suggests that the Raman signals of the 2D-bP are due to flakes with a number of layers greater than or equal to 3–6, in agreement with what is expected from the exfoliation process in the liquid phase [15].

The number of layers in the 2D-bP can also be estimated by the Tauc plot method [39]. The Tauc plot graphs correlate the absorption edge observed in UV-Vis spectra assigned to the high-energy transition (Fig. 1C and D) with the number of layers since both band gap and high-energy transition are thickness-dependent [39]. Fig. S2 in SI reports the Tauc plot of the different suspensions showing that the high energy transitions of 2D-bP space from  $\sim 2.3$  eV (Cyrene),  $\sim 2.5$  eV (NMP) and  $\sim 2.9$  eV (DI water) associated with an estimated band gap between 0.94 to 1.5 eV. Based on Woomer's observations [39] this corresponds to 3–6 layer-2D-bP, slightly thinner for the nanosheets obtained in DI water, having higher energy transition, in agreement with the DLS and Raman experimental data discussed above.

Finally, to better support the evidence regarding the shape and size of 2D-bP, TEM analysis was conducted on the sample exfoliated in DI water. As shown in Fig. S3, the results indicate that the nanoflakes re-aggregated due to their deposition on the support. This resulted in agglomerated structures comprising unordered and unoriented nanoflakes, as well as isolated nanoflakes with sizes ranging from 30 to 100 nm, which is consistent with the DLS analysis. However, stacked and ordered nanostructures were also observed (see yellow square in Fig. S3), indicating the presence of very small particles that had not been exfoliated. Therefore, although DI water does not offer the same exfoliation capability due to its unfavourable chemical and physical properties, NMR analysis of the resulting suspension shows mainly 2D-bP with few oxidized species, indicating good stability of 2D-bP after exfoliation in DI water. In addition, data from DLS, UV-Vis, and Raman

confirm that the quality, size, and thickness of the 2D-bP are comparable to those produced in Cyrene and NMP. However, Cyrene is a green and safe but high-boiling solvent, and NMP is a high-performing solvent but toxic and high-boiling.

### 3.4. Stability and photoactivity of 2D-bP

As mentioned above, the main drawback of 2D-bP, limiting its applications, is the lack of stability in the presence of air and humidity [47,48,59,60]. To evaluate the protective effect of solvation [60], we have monitored the temporal stability of suspensions of 2D-bP exfoliated in DI water and Cyrene. While the solvation and stabilization effect of NMP is well recognized and reported [44,60], Cyrene has never been used as an exfoliating agent for bP so no data can be retrieved. DI water has been used as an exfoliating medium with controversial effects when oxygen is present. It has been reported that 2D-bP is stable in contact with deaerated (i.e.,  $\text{O}_2$ -depleted) water [61,62]. However, these experimental conditions are difficult to maintain, especially during the use of the suspension for the claimed applications. Fig. S4A and B (SI) show the absorbance changes at 466 nm as a function of the time for the two suspensions (in DI water and Cyrene, respectively), obtained and stored in the air in the same experimental conditions. Degradation of the 2D-bP should result in a decrease of the absorbance  $A_{466}\text{-}A_{900}$  over time, which was observed for both solvents. However, we experienced different absorbance decreases for the two samples. In DI water, the normalized absorbance quickly decreased to 14 % (Fig. S4C, SI) of the starting value in 15 days, while in Cyrene it speedily decreased in the first 5 days and then remained stable around 44 % of the starting value up to 40 days tested by maintaining the characteristic absorption even after 60 days (Fig. S4B, SI).

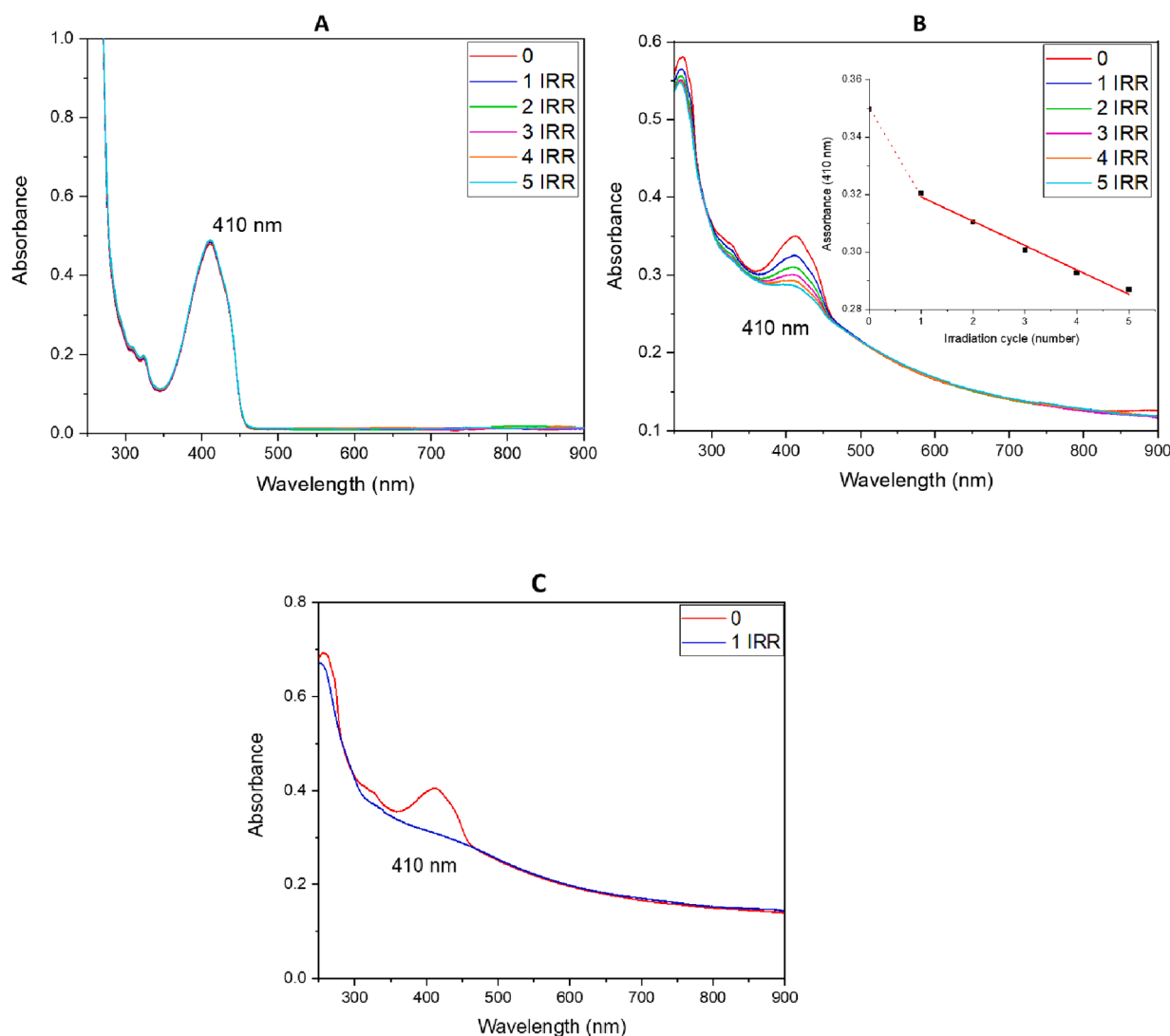
In both solvents, a more pronounced decrease in absorbance was observed in the first 4 days. The fast degradation of 2D-bP observed during the first days can be attributed to a reaction between the surface of the layers and  $\text{O}_2$ , which is present either in the air or dissolved in the solvent, leading to oxidation [49,63]. This reaction gradually turns the hydrophobic pristine 2D-bP surface into a hydrophilic one, thus facilitating the reaction of water-borne oxygen with  $\text{P}^0$  on the surface of 2D-bP [48]. Indeed, theoretical studies suggested that water does not interact with the pristine 2D-bP surface (accounting for the poor capability of water to stabilize nanosheets by solvation); however, the interaction becomes favourable once the surface is oxidized [47]. Even if

oxidized bP is indicated as the most stable species in water (and its actual surface oxidation has little impact on the main structural properties) [64], water can remove  $PxOy$  from the surface exposing  $P^0$  to continued oxidation [50]. This supports the experimental results indicating a faster degradation rate of 2D-bP suspended in DI water than in Cyrene. As far as Cyrene is concerned, based on physicochemical data currently available [29], it can be suggested that due to its aprotic nature, it is affine with hydrophobic substrates, and it does not create hydrogen bonds. Thus, after the first oxidation step probably due to the dissolved oxygen, Cyrene's capacity to interact with oxidized 2D-bP is lower than water and the concentration of 2D-bP remains stable for a longer time, explaining the overall better stability of 2D-bP in Cyrene. The value of oxygen concentration dissolved in Cyrene is currently unknown. Additionally, starting from the fifth day we observed a fast sedimentation for the sample in DI water and the suspension changed colour from light yellow to transparent. Differently, the suspension in Cyrene did not show a significant sedimentation or colour change. By measuring, by DLS, the size dimension of 2D-bP exfoliated in DI water over time we observed an increase in the values (Fig. S4D, SI), suggesting a re-aggregation phenomenon in agreement with the sedimentation effect. This evidence confirms that nanosheets in DI water are not

stabilized by the solvent undergoing regrouping and generating particles that tend to sediment. However, though in Cyrene the particles do not aggregate proving better solvation capacity, our data shows that within the first 4 days after preparation, the behaviour of the two suspensions is similar and only deviates for extended times.

Based on these findings, further experiments were designed aimed at preliminary evaluation of the photoactivity characteristics of 2D-bP. As previously mentioned, 2D-bP has also attracted the attention of researchers thanks to their photosensitizing properties, i.e., the generation of singlet oxygen species following interaction with appropriate wavelengths [65].

The generation of singlet oxygen species is favoured if oxygen is close to a photosensitizer molecule whose energy bandgap fits the redox potential of  $^3O_2/{}^1O_2$  which is in the range 1.6 eV for  ${}^1\Sigma_g^+$  and 0.98 eV for  $\Delta_g$ , having the  ${}^1O_2$  two states [66]. As previously mentioned, bP has a number-of-layer-dependent bandgap, which varies from 0.3 eV to 2 eV, thus falling in the requested energy interval, when properly exfoliated. Then, 2D-bP can act as a light absorber, mediating the energy transfer to oxygen molecules in the surrounding environment by activating the formation of  ${}^1O_2$ . The optimal wavelength range for the photosensitizer activation is below 600 nm (UV-NIR, typical of the phosphorene band



**Fig. 3.** UV-Vis spectra over irradiance cycles of A: DPBF (0.05 mg/mL); B: DPBF in the presence of 2D-bP – suspension obtained from bP exfoliated in DI water with 2D-bP concentration = 0.01 mg/mL, DPBF concentration = 0.02 mg/mL; in the inset the evolution of  $A_{410}$  vs irradiation cycle number; C: DPBF in the presence of 2D-bP – suspension obtained from bP exfoliated in DI water with 2D-bP concentration = 0.01 mg/mL and enriched in oxygen content, DPBF concentration = 0.02 mg/mL. The signal decrease at  $\lambda = 410$  nm is descriptive of the reaction between DPBF and  ${}^1O_2$  as reported in Fig. S4 in SI.



gap), which is called the “optimal therapeutic window” since it covers a therapeutically safe wavelength range of radiations, still having enough energy to allow the transition to the excited singlet state of oxygen [67], without compromising biological tissues.

To assess the photoactivity of 2D-bP in a near-biological environment, we conducted experiments using the water-soluble probe (1,3-diphenylisobenzofuran, DPBF) that could measure the particles' ability to produce singlet oxygen in aqueous suspension. For the nanosheets produced in DI water, the ethanolic solution of the probe was directly added to suspensions, while for particles obtained in Cyrene and/or NMP, separation and re-suspension in water were necessary before solubilizing the trapper. As a result of irradiation, the phosphorus atoms composing flakes absorb light, which is transferred to the oxygen molecules dissolved in the aqueous solution and interacting with P lone pairs, leading to the adsorption of  $O_2$  and generation of  $^1O_2$ .  $^1O_2$  species further react with DPBF through a Diels-Alder 1,4- cycloaddition (Fig. S5, SI). This causes a reduction of the absorption intensity of the characteristic peak of the probe molecule at about 410 nm [65].

According to the experimental settings employed for  $^1O_2$  generation, singlet oxygen production was first studied for the 2D-bP suspension obtained in DI water. Fig. 3 shows the absorption spectra of DPBF (A) and in the presence of 2D-bP (B), both after 5 irradiation cycles, as described in the experimental section.

Although the designed experiments did not allow continuous monitoring of the absorbance over irradiation time, it is evident that the  $A_{410}$  value of DPBF alone (Fig. 3A) does not decrease with irradiation cycles, unlike in the presence of 2D-bP (Fig. 3B): in the latter conditions, singlet oxygen production is promoted and, due to the reaction between DPBF and  $^1O_2$  (Fig. S5, SI), the absorbance at  $\lambda = 410$  nm decreases from 0.35 to 0.28 throughout 5 irradiation cycles, which corresponds to a decrease of initial absorbance equal to  $\approx 20$  %. Additionally, a linear decrease in absorbance is observed at each irradiation cycle, except for the first point where the decrease is greater as shown in the inset of Fig. 4B. Since we did not saturate the solution with oxygen but only left the cuvette in the air during the irradiation and UV analysis phases, it must be assumed that the first cycle benefited from a higher content of oxygen naturally dissolved in the solution. After the first step, and thus at equilibrium, each radiation produces a similar decrease, and therefore similar  $^1O_2$  content as a function of the amount of solubilized oxygen. It is known that DPBF has a high sensitivity towards  $^1O_2$ , trapping up to 50 % of all  $^1O_2$  present [68]. Given that DPBF and  $^1O_2$  react with a stoichiometric ratio and assuming that, under our conditions, the number of moles of DPBF that bleach during irradiation is half of the total amount of  $^1O_2$  produced, we can estimate the yield of moles of  $^1O_2$  that are formed from our initial 2D-bP concentration (Table S2 in SI).

From the values reported in Table S2, it can be estimated that, except for the first irradiation cycles, in the subsequent ones, the number of moles of DPBF that react and, therefore, the number of moles of  $^1O_2$  produced, are quite constant (with a weak decrement), demonstrating the photocatalytic behaviour of 2D-bP. In this condition, the total amount of  $^1O_2$  produced over the irradiation experiment, calculated as the total of  $^1O_2$  produced in each cycle, was equal to  $1.75 \times 10^{-4}$  mg. This quantity has been produced from a starting amount of 2D-bP of about 0.02 mg.

Therefore, the  $^1O_2$  production depends on the amount of molecular oxygen in the surrounding environment. To better highlight this effect, a DI water suspension of 2D-bP added with proper DPBF quantity was bubbled with pure  $O_2$  flow, to enrich the solution in oxygen and the change of the DPBF absorbance at 410 nm after irradiation was collected. The absorption of DPBF dramatically decreased after only one irradiation cycle (Fig. 3C) and no detectable signal ascribable to DPBF was noticed. This oxygen content-dependent behaviour clearly confirms that the  $^1O_2$  is generated under the photosensitizing process by energy transfer from 2D-bP to ground state  $O_2$ .

Finally, to assess that no phosphorene oxidation/degradation occurs during the irradiation of 2D-bP suspension, experiments were designed

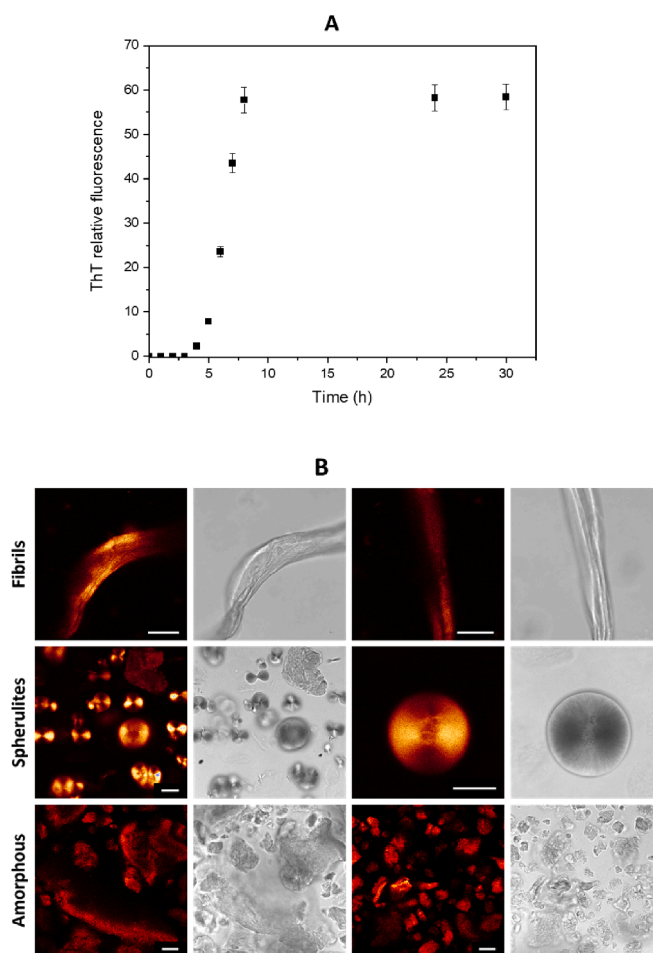


Fig. 4. A: ThT fluorescence assay of 2.5 mg/mL of human insulin in 20 % acetic acid and 25 mM NaCl, pH 2.0 at 60 °C and 600 rpm; B: Confocal fluorescence (columns 1 and 3) and transmission (columns 2 and 4) images of insulin aggregates with different morphologies after ThT staining. Scale bars: 25  $\mu$ m.

and conducted to test the irradiation stability of 2D-bP. We measured the absorbance of two aliquots of 2D-bP suspension in DI water at 466 nm ( $A_{466}$ - $A_{900}$  values) over time: one aliquot was kept at room temperature and the other one was subjected to 5 irradiation cycles before each UV measurement. Fig. S6 (SI), reports the change in absorbance. The decrease in 2D-bP content appears to follow a constant trend regardless of whether the sample was exposed to irradiation or not. This suggests that the 2D-bP content variation over time is independent of irradiation and that the previously described degradation/oxidation pathway is not affected by light. These data also prove that singlet oxygen generation occurs by mere energy transfer without structural detriment of 2D-bP. Therefore we can assume that, in our conditions, no degradation or oxidation was induced by light, differently from that reported in other studies [69,47]. Regarding the chosen applications, this means that the 2D-bP content, although decreasing over time, is not influenced by radiation. We can observe that after 20 days, the DI aqueous suspension of 2D-bP shows a UV-Vis absorbance value close to zero (less than 0.02). Interestingly, by performing an irradiation experiment on this sample, a significant decrease in DPBF absorbance was monitored. Fig. S7 (SI) shows the results of an irradiation experiment performed on a 20-day-old 2D-bP DI water suspension. After 5, 15 and 25 irradiation cycles an aliquot of DPBF has been added each time, to measure the effective production of  $^1O_2$ . It was surprising to observe that even after 45 irradiation cycles, 2D-bP showed moderate photoactivity and it was still able to produce  $^1O_2$ . This confirms that 2D-bP has a distinct ability to act as a photosensitizer, even in small concentrations;

besides, it cannot be excluded that the partially or minimally oxidized 2D-bP species present a certain photoactivity.

To test the photoactivity of the 2D-bP exfoliated in NMP or Cyrene, the suspensions were centrifuged at 14000 rpm and the precipitate re-dispersed in DI water. The particles obtained in NMP or Cyrene showed similar photoactivity (Fig. S8 SI), but their concentration after centrifugation was lower than the initial one obtained at the end of the exfoliation procedure: from 30 to 21 mg/L for those obtained in NMP and from approximately 18 to 9 mg/L for those exfoliated in Cyrene. This outcome is due to solvent removal procedure, which prevents 2D-bP from being completely recovered and confirms that the exfoliation process in DI water is advantageous if targeted for applications in aqueous solutions.

### 3.5. 2D-bP in insulin amyloid aggregation

The abnormal aggregation of proteins and peptides into insoluble amyloid fibrils is associated with the development of various neurodegenerative diseases (e.g. Alzheimer's disease) and metabolic disorders (e.g. diabetes). Insulin is a small peptide hormone produced in the  $\beta$  cells of the pancreatic islets of Langerhans and an important therapeutic protein for type II diabetes conditions. Due to its broad therapeutic use in the treatment of diabetes, the propensity of insulin to self-assemble into amyloid fibrils decreases the efficacy of insulin administration by interfering with its delivery and causing diabetic ketoacidosis, a life-threatening complication.

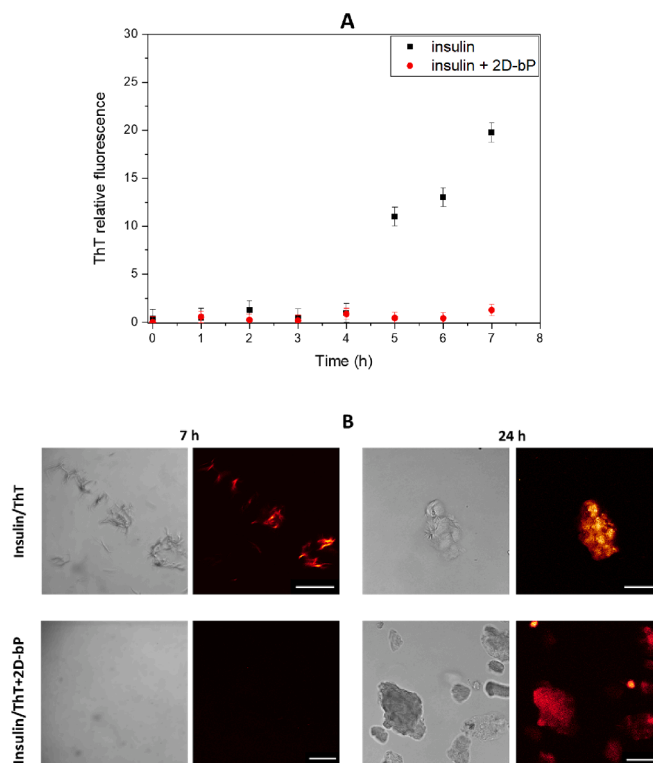
Similarly, to other amyloidogenic peptides, the kinetics of aggregation of insulin into amyloid structures can be described by a sigmoidal curve presenting three typical phases: the lag phase during which the protein misfolds and begins to self-assembly into small oligomers, the elongation phase where the amyloid fibrils are rapidly formed and the saturation phase when mature amyloid structures are stable [70,12,71].

Fig. 4A shows the typical time course of insulin fibrillogenesis measured by ThT fluorescence assay as described in the methods. ThT is an extrinsic benzylamine/benzothiazole fluorescent dye that can specifically intercalate between the cross- $\beta$  structure of the amyloid fibrils. Upon binding it undergoes a strong fluorescence enhancement, therefore its fluorescence intensity can be directly correlated to the content of fibrils [72].

To qualitatively evaluate the morphology of the biggest fibrillar species formed in the final phase after 24 h, a confocal microscopy study was performed on aliquots of the insulin solution used for the aggregation kinetics experiments. At the plateau, many amyloid structures intensely stained by ThT could be observed (Fig. 4B). Insulin aggregates sometimes appear as long fibril bundles (10–50  $\mu\text{m}$ ), but aggregates with different morphologies are often present in the same sample. The shape of these aggregates (that often converge in large superstructures) can be fibrillar, amorphous or even spherical (spherulites), like the structures described by Biancalana *et al* [72].

Before investigating the effects of 2D-bP on the insulin aggregation process, we checked the stability of 2D-bP over time in the fibrillogenesis conditions, i.e., in an aqueous solution of 20 % acetic acid at 60  $^{\circ}\text{C}$ . After almost five hours, there was a significant decrease in the ( $A_{466-A900}$ ) absorbance ratio, indicating that the nanosheets underwent a degradation process (Fig. S9). In agreement with Chen *et al.* [73] the reactive  $-\text{COOH}$  groups can accelerate the process of  $\text{O}_2$  adsorption on the 2D-bP surface by lowering the reaction barrier of  $\text{O}_2$  with dangling P atoms, thus increasing the production rate of intermediates, i.e., organic phosphorus ( $\text{CH}_3\text{O}_5\text{P}$ ) that evolve in phosphate and phosphonates.

Fig. 5A shows the aggregation kinetics of insulin with and without 2.5  $\mu\text{g}/\text{mL}$  of 2D-bP. 2D-bP significantly inhibited the formation of amyloid structures in the first 7 h. After 24 h, both samples reached almost the same ThT fluorescence intensities (data not shown) indicating that the insulin self-assembly could no longer be blocked by 2D-bP probably due to nanoflakes degradation, as discussed above. This result was also confirmed by confocal experiments: after 7 h no amyloid structure was



**Fig. 5.** A: ThT fluorescence assay of 2.5 mg/mL of human insulin alone (blue) and in the presence of 2.5  $\mu\text{g}/\text{mL}$  of 2D-bP in 20 % acetic acid and 25 mM NaCl, pH 2.0 at 60  $^{\circ}\text{C}$  and 600 rpm; B: Confocal fluorescence (columns 2 and 4) and transmission (columns 1 and 3) images of insulin aggregates with and without incubation with 2D-bP at different times after ThT staining. Scale bars: 50  $\mu\text{m}$ . (For interpretation of the references to colour in this figure legend, the reader is referred to the web version of this article.)

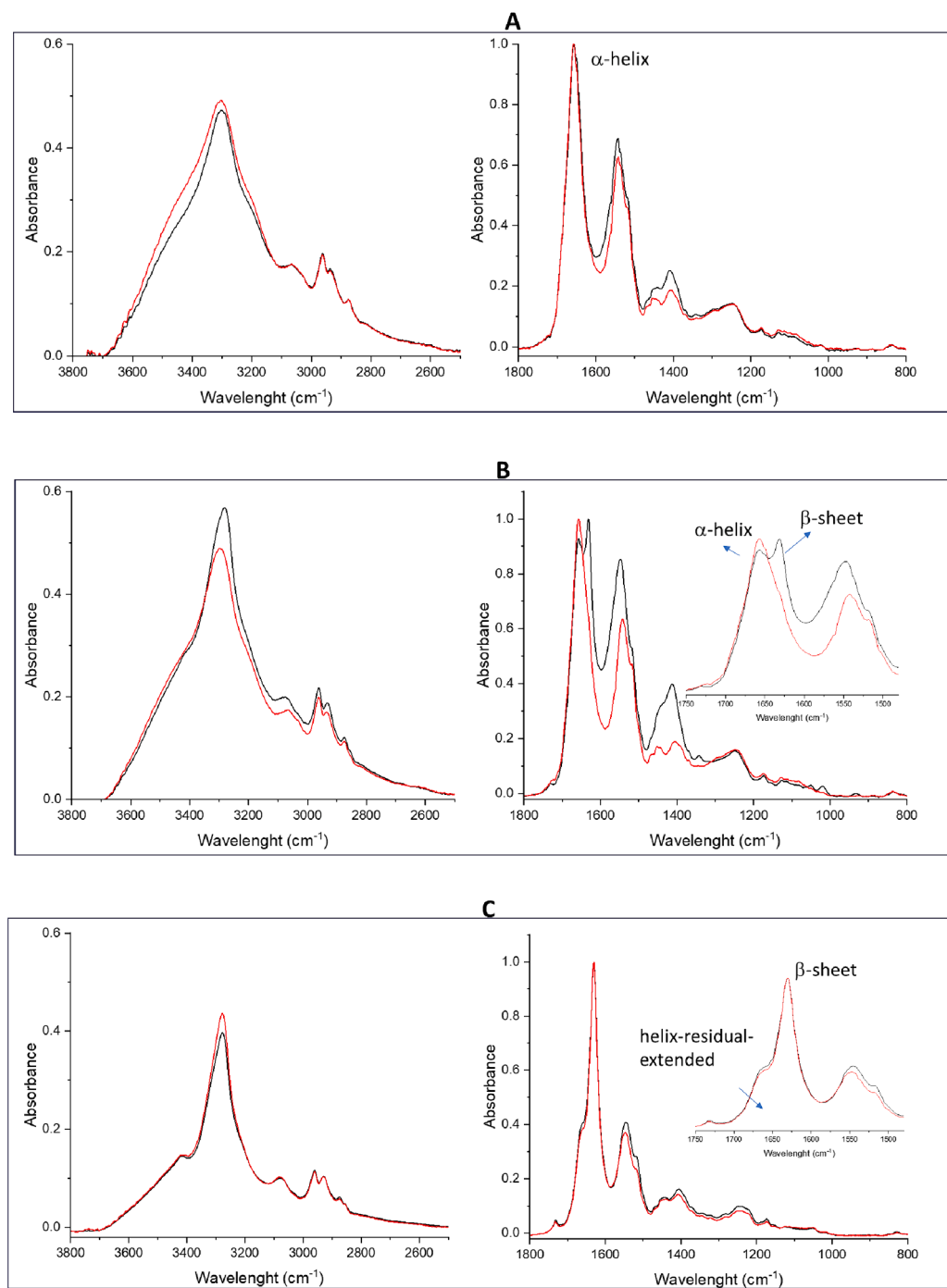
detected in the sample treated with 2D-bP, while at 24 h many intensely emitting aggregates stained by ThT were revealed in both the treated and control samples (Fig. 5B).

The secondary structures of the different species of insulin during the aggregation kinetics were investigated using FTIR-ATR spectroscopy with and without 2D-bP. Fig. 6 shows the ATR-FTIR spectra of insulin sampled at  $t = 0$  (A panel), after 7 h (B panel) and 24 h (C panel) with (red line) and without (black line) 2D-bP.

It is known that the secondary structure of native insulin is basically  $\alpha$ -helix with portions of  $\beta$ -sheet ribbons and  $\beta$ -turns [74]. This is confirmed by ATR-FTIR spectra at  $t = 0$  (with or without 2D-bP) showing the Amide I peak at 1656  $\text{cm}^{-1}$ . After 7 h incubation in aggregating condition, the insulin sample without 2D-bP shows the formation of extended  $\beta$ -sheet structures clearly demonstrated by the increase of the peak at 1631  $\text{cm}^{-1}$ , along with residual  $\alpha$ -helix, while the sample incubated with 2D-bP is characterized only by the Amide I peak at 1656  $\text{cm}^{-1}$ . After 24 h both protein samples with and without 2D-bP show mainly  $\beta$ -sheets, confirming the results of ThT assay.

In order to gain further insights into the conformational changes, we performed the spectral deconvolution of the Amide I band, which is the most reliable absorption widely employed to investigate quantitatively the changes in the secondary structure [35,36]. Table 2 summarizes the quantitative results of the secondary structure of insulin in all conditions studied.

The band at 1655–1658  $\text{cm}^{-1}$  is due to  $\alpha$ -helical structures buried/not-solvated, and the component around 1678–1985  $\text{cm}^{-1}$  is associated with turn structures [75,76]. The band at 1628–1630  $\text{cm}^{-1}$  is assigned to intramolecular  $\beta$  sheets. The bands at 1690 and 1602–1615  $\text{cm}^{-1}$  are assigned to anti-parallel  $\beta$ -sheets and intermolecular  $\beta$ -sheets [77]. Absorptions at 1660  $\text{cm}^{-1}$  are associated with portions of extended



**Fig. 6.** ATR-FTIR spectra of insulin sampled at  $t = 0$  (A panel), after 7 h (B panel; inset enlargement of Amides region) and 24 h (C panel, inset enlargement of Amides region) with (red line) and without (black line) 2D-bp. (For interpretation of the references to colour in this figure legend, the reader is referred to the web version of this article.)

helices exposed to solvent in acid environments [78]. The maximum absorption of the secondary structure mentioned above may change depending on the exposure of the various portions of proteins to solvents and pH [77].

Insulin at  $t = 0$  has a high percentage of  $\alpha$ -helix (76 %, component at  $1655 \text{ cm}^{-1}$ ),  $\beta$  turns (16 %, component at  $1686 \text{ cm}^{-1}$ ) and small fractions of  $\beta$ -structures according to the literature [74]. At  $t = 0$  the addition of 2D-bp in the solution gives a conformational change reducing the  $\alpha$ -helix percentage from 76 to 56 % and increasing beta structures (bands at  $1628 \text{ cm}^{-1}$ ). This result is suggestive of the prompt interaction of 2D-bp with the protein. After 7 h incubation in aggregating conditions

without 2D-bp  $\alpha$ -helix percentage decreased to 41 % and  $\beta$  structures globally reached almost 60 % including both intramolecular and intermolecular  $\beta$ -sheets. Intermolecular  $\beta$ -sheets with components at around  $1605\text{--}1630 \text{ cm}^{-1}$  are typical of aggregate structures. In the solution containing 2D-bp the band at  $1658 \text{ cm}^{-1}$  assigned to  $\alpha$ -helix decreased to 26 % but ATR-FTIR analysis evidenced a component at  $1640 \text{ cm}^{-1}$  representing 46 % assigned to unordered structure. Thus, 2D-bp avoids the formation of organized  $\beta$ -sheet structures, which is preliminary to the formation of fibrils.

After 24 h incubation time, 2D-bp degraded, as reported above, and their antiaggregating property failed. In these solutions, insulin

**Table 2**

Summary of the secondary structure analysis of insulin samples at  $t = 0, 7$  h and 24 h during the aggregation kinetics with and without 2D-bP. Wavenumber in  $\text{cm}^{-1}$  and the secondary structure % between brackets are reported.

Insulin $t = 0$	Insulin/2D-bP	Insulin $t = 7$ h	Insulin/2D-bP	Insulin $t = 24$ h	Insulin/2D-bP	Assignment
1618 (3.9 %)	1628 (26.4 %)	1602 (19.4 %) 1615 (6.6 %)	1612 (3.2 %)	1603 (14.5 %) 1613 (7.1 %)	1603 (14.2 %) 1614 (7.3 %)	$\beta$ -Sheets (intermolecular)
		1628 (28.0 %)		1630 (52.3 %)	1630 (53.6 %)	$\beta$ -Sheets (intramolecular)
			1640 (46.1 %)			Unordered structure
1655 (75.9 %)	1657 (56.4 %)	1656 (41.0 %)	1658 (26.3 %)	1657 (26.1 %)	1658 (24.9 %)	$\alpha$ -Helix
1660 (4.4 %)	1660 (3.9 %)					extended Helix
1686 (15.9 %)	1685 (13.2 %)		1678 (24.5 %)			$\beta$ -Turns
		1690 (5 %)				Antiparallel $\beta$ -sheets

molecules are characterized by  $\beta$ -sheet structures (about 75 %) with or without 2D-bP. Fig. S10 shows the trend of  $\beta$ -structure % (including intramolecular, intermolecular  $\beta$ -sheets and  $\beta$ -turns) vs insulin incubation time with or without 2D-bP.

### 3.6. 2D-bP in insulin fibrils disaggregation

Finally, we performed a preliminary investigation on the possible effects of 2D-bP on insulin fibril disaggregation. For these experiments, 2 mg/mL of mature insulin fibrils prepared as above described were incubated or not with 2.5  $\mu\text{g}/\text{mL}$  2D-bP DI water suspensions for 5 days, and stored at 4  $^{\circ}\text{C}$ . The insulin fibril solutions were centrifuged at 5000 rpm for 5 min to remove larger aggregates potentially interfering with spectroscopic measurements and the experiments were performed on supernatants.

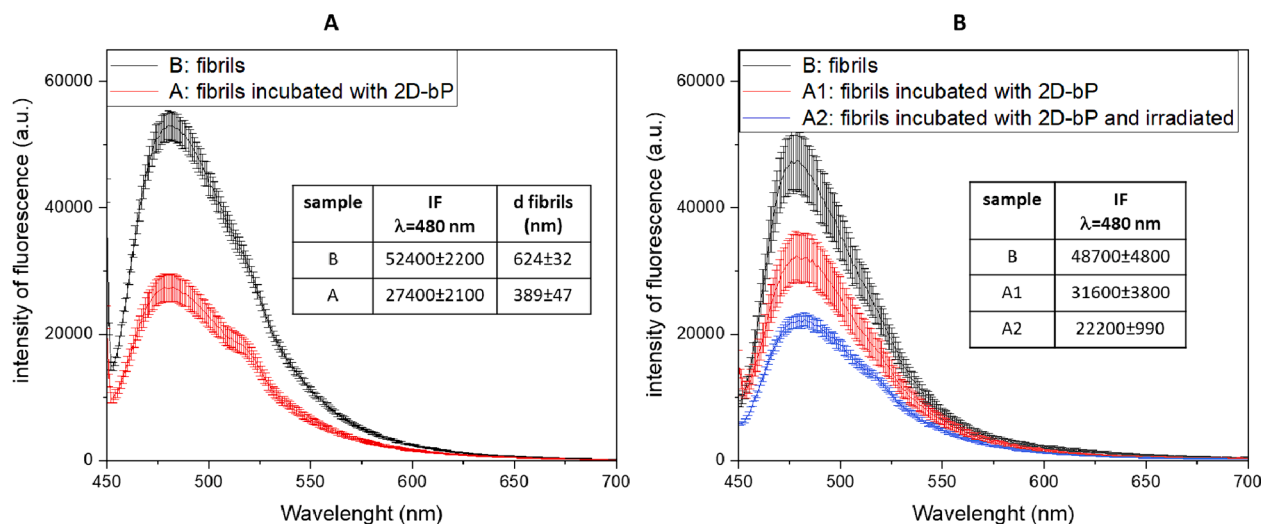
ThT assay was then employed to measure the degree of aggregation of samples treated and untreated with 2D-bP, and, on the same solutions, DLS measurements were also performed to determine the average particle size. Fig. 7A and data in the inset show that the fluorescence intensity (I.F.) of ThT decreased by about 47 % according to a decrease in fibrils concentration. DLS data reported in the inset table also showed that the main diameters of aggregates remarkably decreased. Moreover, considering that the insulin molecule has a molecular diameter of  $\sim 2.7$  nm [79], the aggregates seem to be reduced from 208 to 141 building blocks.

These results are encouraging because they suggest that 2D-bP have the potential to depolymerize mature fibrils, despite the possible acid degradation. Regarding the 2D-bP damage, it should be noted that the polymeric embedding of the 2D-bP due, in this case, to the apolar

interaction with the proteins (fibrils), might have protected/passivated the bP layer surfaces from degradation, as well-established in the literature, even for polymeric matrices of a different nature [52,80]. However, we cannot completely rule out the possibility of a different fibril's aggregate concentration in the samples, owing to the fractionation (by centrifugation) of disparate populations induced by the 2D-bP. To exclude this possibility and to test the photoactivity of 2D-bP in mature fibril disaggregation, a different experiment was designed. Sample A and B having the same fibril concentration were added with the same volume of 2D-bP DI water suspension or DI water alone, respectively. Sample A was divided into two portions (samples A1 and A2) having the same concentration of fibrils and 2D-bP and the A2 aliquot was irradiated to generate singlet oxygen. ThT fluorescence measurements (Fig. 7B) showed that the formation of singlet oxygen remarkably ameliorated the fibrils disaggregation, with a decrease of about 55 % of fluorescence intensity with respect to sample of fibrils alone (sample B) and of about 30 % with respect to the sample containing the same concentration of 2D-bP but not-irradiated (sample A1). The Fluorescence Intensity (IF) value of the latter decreased by about 32 % with respect to sample B (mature fibrils alone) confirming that the disaggregating effect can be induced by 2D-bP, even after only one day of incubation.

## 4. Conclusions

Successful liquid-phase exfoliation of bP was achieved in Cyrene, a novel bio-based and biocompatible solvent previously unexplored for bP exfoliation, as well as in DI water, a primary medium for bP nanolayer applications in the biomedical field. For comparison, the same



**Fig. 7.** A: Fluorescence emission spectra ( $\lambda_{\text{exc}} = 442$  nm) of 25  $\mu\text{M}$  ThT in the presence of insulin fibrils (black) and 2D-bP incubated (5 days) insulin fibrils (red). Intensity of fluorescence (I.F.) in arbitrary units (a.u.). Inset: I.F. and DLS data. B: Fluorescence emission spectra ( $\lambda_{\text{exc}} = 442$  nm) of 25  $\mu\text{M}$  ThT in the presence of insulin fibrils (black), 2D-bP incubated (24 h) insulin fibrils (red), 2D-bP-incubated insulin fibrils after irradiation (25 cycles, blue curve). Inset: I.F. data. (For interpretation of the references to colour in this figure legend, the reader is referred to the web version of this article.)



exfoliation process was also carried out in NMP, which is a high-performing solvent for bP exfoliation but is toxic and harmful to health and the environment, making it questionable for use in the medical field. The obtained suspensions were analysed using a range of techniques, including DLS, ICP-OES,  $^{31}\text{P}$  Solid State NMR, UV-Vis, TEM and Raman spectroscopies, to study the structural features of the resulting 2D-bP and monitor their stability over time.

The exfoliation yield data in the three solvents (NMP > Cyrene > DI water) were discussed analysing their chemical and physical characteristics based on Hansen parameters, density and viscosity. We found that the surface tension of all three solvents was strong enough to overcome the van der Waals forces between the layers (40 mJ/m). However, the polar and protic nature of DI water negatively impacted the stabilization process of nanoflakes (after exfoliation), whose surface has a hydrophobic nature. Compared to NMP and Cyrene, DI water lacks efficiency in interacting with the surface of 2D-bP. As a result, it fails to produce a sufficient solvation effect, leading over time to the deposition of bP nanolayers and their subsequent degradation through oxidative processes due to the high oxygen solubility in water. On the other hand, NMP and Cyrene exhibit good solvation properties (indicated by their Hansen parameter values, which are more similar to those of bP). Furthermore, these solvents have higher density and viscosity values, which ensure greater stability of the suspensions obtained, inhibiting re-aggregation effects. However, despite the lower yield, exfoliation in DI water provided 2D-bP with structure and size similar to those obtained in the other solvents and with short-time stability to oxidation comparable to that obtained in Cyrene: the suspensions stored in air showed degradation with a similar trend in the first 5 days. The photoactivity of the 2D-bP obtained in DI water was then investigated by directly irradiating the aqueous suspensions within the therapeutic window after solubilization of appropriate amounts of singlet oxygen trapper. The bP nanolayers showed a good ability to generate singlet oxygen over successive irradiation cycles (with about 0.09 mg of  $^1\text{O}_2$  produced for 1 mg of 2D-bP in 2.5 mL of water left in the air) and this capability was retained even for extremely low concentrations (less than 1 mg/L). It has also been demonstrated that the irradiation process did not accelerate the degradation or oxidation of the bP nanolayers, indicating that they serve merely as photosensitizers and that the interaction with molecular oxygen occurs only in view of singlet oxygen formation. Although similar data were collected using 2D-bP obtained in Cyrene or NMP, a mandatory separation from the high-boiling solvents and subsequent re-dispersion in DI water was necessary. This process led to a decrease in the starting concentration and then thwarted the higher exfoliation yields. Additionally, the unavoidable residual content of solvents on 2D-bP surfaces couldn't be avoided. Moreover, by considering that insulin administration for diabetes treatment is often hindered by the tendency of insulin to self-assemble into amyloid fibrils, we investigated the effects of bP nanolayers, directly obtained in DI water, to inhibit the aggregation of insulin fibrils or promote their disaggregation. The results were significant, showing that 2D-bP were effective at intercalating within the aggregates or between the fibrils, inhibiting the aggregation or provoking disassembling. This effect is enhanced by the irradiation in the conditions used for singlet oxygen production, definitively proving the potential exploitation of these systems in photodynamic therapeutic applications.

The findings of this study are significant as they demonstrate that the production of 2D-bP in safe and biocompatible solvents under appropriate conditions is feasible. Specifically, by using DI water, it is possible to generate bP nanolayers with dimensions and structural features that are appropriate for direct usage in biomedical applications. Although the stability of these particles must be further investigated and improved, they have shown promising results compared to the expected targets.

## CRediT authorship contribution statement

**Carla Caponio:** Methodology, Investigation, Formal analysis, Data curation. **Agata Costanzo:** Investigation, Data curation. **Serena Coiai:** Writing – review & editing, Validation, Conceptualization. **Francesca Cicogna:** Writing – review & editing, Validation, Conceptualization. **Emanuela Pitzalis:** Investigation, Data curation. **Silvia Borsacchi:** Methodology, Investigation. **Giulia Lorenzetti:** Methodology, Investigation. **Emilia Bramanti:** Writing – review & editing, Writing – original draft, Validation, Methodology, Investigation, Data curation, Conceptualization. **Alessia Papalini:** Validation, Methodology, Investigation, Data curation. **Antonella Battisti:** Visualization, Methodology, Investigation. **Antonella Sgarbossa:** Visualization, Methodology, Investigation, Writing – review & editing, Validation, Data curation, Conceptualization. **Elisa Passaglia:** Writing – review & editing, Writing – original draft, Validation, Supervision, Project administration, Methodology, Investigation, Funding acquisition, Conceptualization.

## Declaration of competing interest

The authors declare the following financial interests/personal relationships which may be considered as potential competing interests: Elisa Passaglia Emilia Bramanti Silvia Borsacchi report equipment, drugs, or supplies were provided by Tuscany Region and CISUP (Centre for Instrument Sharing-University of Pisa). If there are other authors, they declare that they have no known competing financial interests or personal relationships that could have appeared to influence the work reported in this paper.

## Data availability

All data are available in the main file and/or in [supporting information](#).

## Acknowledgements

E.P. and E.B. acknowledge Regione Toscana POR FESR 2014-2020 for the project FELIX (Fotonica ed Elettronica Integrate per l'Industria), Grant Number 6455 for providing the facilities Horiba FluoroMax-4 spectrofluorometer. S.B. acknowledges CISUP (Centre for Instrument Sharing-University of Pisa) for the use of the Bruker Avance NEO Solid State NMR spectrometer. Dr. Enrico Berretti is acknowledged for TEM analysis.

## Appendix A. Supplementary data

Supplementary data to this article can be found online at <https://doi.org/10.1016/j.flatc.2024.100665>.

## References

- [1] Y. Zhu, Z. Xie, J. Li, Y. Liu, C. Li, W. Liang, W. Huang, J. Kang, F. Cheng, L. Kang, O. A. Al-Hartomy, A. Al-Ghamdi, S. Wageh, J. Xu, D. Li, H. Zhang, From phosphorus to phosphorene: applications in disease therapeutics, *Coord. Chem. Rev.* 446 (2021), <https://doi.org/10.1016/j.ccr.2021.214110>.
- [2] M. Luo, T. Fan, Y. Zhou, H. Zhang, L. Mei, 2D Black Phosphorus-Based Biomedical Applications, *Adv. Funct. Mater.* 29 (2019), <https://doi.org/10.1002/adfm.201808306>.
- [3] S.K. Gaddam, R. Pothu, A. Saran, R. Boddula, Biomedical applications of black phosphorus, *Eng. Mater.* (2020) 117–138, [https://doi.org/10.1007/978-3-030-29555-4\\_6](https://doi.org/10.1007/978-3-030-29555-4_6).
- [4] J.R. Choi, K.W. Yong, J.Y. Choi, A. Nilghaz, Y. Lin, J. Xu, X. Lu, Black phosphorus and its biomedical applications, *Theranostics* 8 (2018) 1005–1026, <https://doi.org/10.7150/thno.22573>.
- [5] M. Tatullo, F. Genovese, E. Aiello, M. Amantea, I. Makeeva, B. Zavan, S. Rengo, L. Fortunato, Phosphorene is the new graphene in biomedical applications, *Materials* 12 (2019), <https://doi.org/10.3390/ma12142301>.
- [6] Y. Li, Z. Du, X. Liu, M. Ma, D. Yu, Y. Lu, J. Ren, X. Qu, Near-infrared activated black phosphorus as a nontoxic photo-oxidant for Alzheimer's amyloid- $\beta$  peptide, *Small* 15 (2019) 1901116, <https://doi.org/10.1002/sml.201901116>.

- [7] M. Qiu, W.X. Ren, T. Jeong, M. Won, G.Y. Park, D.K. Sang, L.-P. Liu, H. Zhang, J. S. Kim, Omnipotent phosphorene: a next-generation, two-dimensional nanoplatform for multidisciplinary biomedical applications, *Chem. Soc. Rev.* 47 (2018) 5588–5601, <https://doi.org/10.1039/C8CS00342D>.
- [8] 2020 Alzheimer's disease facts and figures, *Alzheimer's & Dementia* 16 (2020) 391–460. <https://doi.org/10.1002/alz.12068>.
- [9] J. Yang, W. Liu, Y. Sun, X. Dong, LVFFARK-PEG-stabilized black phosphorus nanosheets potentially inhibit amyloid- $\beta$  fibrillogenesis, *Langmuir* 36 (2020) 1804–1812, <https://doi.org/10.1021/acs.langmuir.9b03612>.
- [10] N. Wu, X. Wang, C.M. Das, M. Ma, N. Qiao, T. Fan, H. Zhang, G. Xu, K.-T. Yong, Bioengineering applications of black phosphorus and their toxicity assessment, *Environ. Sci. Nano* 8 (2021) 3452–3477, <https://doi.org/10.1039/D1EN00273B>.
- [11] X. Zhang, I.S. Donskyi, W. Tang, S. Deng, D. Liu, S. Zhang, Q. Zhao, B. Xing, Biological effects of black phosphorus nanomaterials on mammalian cells and animals, *Angew. Chem. Int. Ed.* 62 (2023), <https://doi.org/10.1002/anie.202213336>.
- [12] S. Wang, C. Li, Y. Xia, S. Chen, J. Robert, X. Banquy, R. Huang, W. Qi, Z. He, R. Su, Nontoxic black phosphorus quantum dots inhibit insulin amyloid fibrillation at an ultralow concentration, *Iscience* 23 (2020) 101044, <https://doi.org/10.1016/j.isci.2020.101044>.
- [13] S. Lin, Y. Chui, Y. Li, S.P. Lau, Liquid-phase exfoliation of black phosphorus and its applications, *FlatChem* 2 (2017) 15–37, <https://doi.org/10.1016/j.flatc.2017.03.001>.
- [14] Y. Zhang, H. Wang, Z. Luo, H.T. Tan, B. Li, S. Sun, Z. Li, Y. Zong, Z.J. Xu, Y. Yang, K.A. Khor, Q. Yan, An air-stable densely packed phosphorene-graphene composite toward advanced lithium storage properties, *Adv. Energy Mater.* 6 (2016) 1600453, <https://doi.org/10.1002/aenm.201600453>.
- [15] S.C. Dhanabalan, J.S. Ponraj, Z. Guo, S. Li, Q. Bao, H. Zhang, Emerging trends in phosphorene fabrication towards next generation devices, *Adv. Sci.* 4 (2017) 1600305, <https://doi.org/10.1002/advs.201600305>.
- [16] J. Cheng, L. Gao, T. Li, S. Mei, C. Wang, B. Wen, W. Huang, C. Li, G. Zheng, H. Wang, H. Zhang, Two-dimensional black phosphorus nanomaterials: emerging advances in electrochemical energy storage science, *Nanomicro Lett.* 12 (2020) 179, <https://doi.org/10.1007/s40820-020-00510-5>.
- [17] G. Sansone, L. Maschio, D. Usvyat, M. Schütz, A. Karttunen, Toward an accurate estimate of the exfoliation energy of black phosphorus: a periodic quantum chemical approach, *J. Phys. Chem. Lett.* 7 (2016) 131–136, <https://doi.org/10.1021/acs.jpcclett.5b02174>.
- [18] M. Schütz, L. Maschio, A.J. Karttunen, D. Usvyat, Exfoliation energy of black phosphorus revisited: a coupled cluster benchmark, *J. Phys. Chem. Lett.* 8 (2017) 1290–1294, <https://doi.org/10.1021/acs.jpcclett.7b00253>.
- [19] A. Rabie Baboukani, I. Khakpour, V. Drozd, C. Wang, Liquid-based exfoliation of black phosphorus into phosphorene and its application for energy storage devices, *Small Struct* 2 (2021) 2000148, <https://doi.org/10.1002/sstr.202000148>.
- [20] L. Chen, G. Zhou, Z. Liu, X. Ma, J. Chen, Z. Zhang, X. Ma, F. Li, H.-M. Cheng, W. Ren, Scalable clean exfoliation of high-quality few-layer black phosphorus for a flexible lithium ion battery, *Adv. Mater.* 28 (2016) 510–517, <https://doi.org/10.1002/adma.201503678>.
- [21] C.P. Bartus, T. Hegedűs, G. Kozma, I. Szent, R. Vajtai, Z. Kónya, Á. Kukovecz, Exfoliation of black phosphorus in isopropanol-water cosolvents, *J. Mol. Struct.* 1260 (2022) 132862, <https://doi.org/10.1016/j.molstruc.2022.132862>.
- [22] J. Kang, S.A. Wells, J.D. Wood, J.-H. Lee, X. Liu, C.R. Ryder, J. Zhu, J.R. Guest, C. A. Husko, M.C. Hersam, Stable aqueous dispersions of optically and electronically active phosphorene, in: *Proceedings of the National Academy of Sciences* 113, 2016, pp. 11688–11693, <https://doi.org/10.1073/pnas.1602215113>.
- [23] J. Shen, L. Liu, W. Huang, K. Wu, Polyvinylpyrrolidone-assisted solvent exfoliation of black phosphorus nanosheets and electrochemical sensing of p-nitrophenol, *Anal. Chim. Acta* 1167 (2021) 338594, <https://doi.org/10.1016/j.aca.2021.338594>.
- [24] N.A. Stini, P.L. Gkizis, C.G. Kokotos, Cyrene: a bio-based novel and sustainable solvent for organic synthesis, *Green Chem.* 24 (2022) 6435–6449, <https://doi.org/10.1039/D2GC02332F>.
- [25] D. Kong, A.V. Dolzhenko, Cyrene: a bio-based sustainable solvent for organic synthesis, *Sustain. Chem. Pharm.* 25 (2022) 100591, <https://doi.org/10.1016/j.scp.2021.100591>.
- [26] S.L., D.Z., R.E., J.N. Waaijers-van der Loop, Toxicity screening of potential bio-based Polar Aprotic Solvents (PAS), *Methodology* 5 (2018) 1.
- [27] A. Citarella, A. Amenta, D. Passarella, N. Micalé, Cyrene: a green solvent for the synthesis of bioactive molecules and functional biomaterials, *Int. J. Mol. Sci.* 23 (2022) 15960, <https://doi.org/10.3390/ijms232415960>.
- [28] C. Grune, J. Thamm, O. Werz, D. Fischer, Cyrene™ as an alternative sustainable solvent for the preparation of poly(lactic-co-glycolic acid) nanoparticles, *J. Pharm. Sci.* 110 (2021) 959–964, <https://doi.org/10.1016/j.xphs.2020.11.031>.
- [29] J. Fernandes, S.S. Nemala, G. De Bellis, A. Capasso, Green solvents for the liquid phase exfoliation production of graphene: the promising case of cyrene, *Front. Chem.* 10 (2022), <https://doi.org/10.3389/fchem.2022.878799>.
- [30] S. Tkachev, M. Monteiro, J. Santos, E. Placidi, M. Ben Hassine, P. Marques, P. Ferreira, P. Alpuim, A. Capasso, Environmentally friendly graphene inks for touch screen sensors, *Adv. Funct. Mater.* 31 (2021), <https://doi.org/10.1002/adfm.202103287>.
- [31] J. Adam, M. Singh, A. Abdvakhidov, M.R. Del Sorbo, C. Feoli, F. Hussain, J. Kaur, A. Mirabella, M. Rossi, A. Sasso, M. Valadan, M. Varra, G. Rusciano, C. Altucci, The effectiveness of cyrene as a solvent in exfoliating 2D TMDs nanosheets, *Int. J. Mol. Sci.* 24 (2023) 10450, <https://doi.org/10.3390/ijms241310450>.
- [32] M. Köpf, N. Eckstein, D. Pfister, C. Grotz, I. Krüger, M. Greiwe, T. Hansen, H. Kohlmann, T. Nilges, Access and in situ growth of phosphorene-precursor black phosphorus, *J. Cryst. Growth* 405 (2014) 6–10, <https://doi.org/10.1016/j.jcrysgro.2014.07.029>.
- [33] F. Martini, S. Borsacchi, G. Barcaro, M. Caporali, M. Vanni, M. Serrano-Ruiz, M. Geppi, M. Peruzzini, L. Calucci, Phosphorene and black phosphorus: the <sup>31</sup>P NMR view, *J. Phys. Chem. Lett.* 10 (2019) 5122–5127, <https://doi.org/10.1021/acs.jpcclett.9b01788>.
- [34] E. Bramanti, M. Bramanti, P. Stiavetti, E. Benedetti, A frequency deconvolution procedure using a conjugate gradient minimization method with suitable constraints, *J. Chemom.* 8 (1994) 409–421, <https://doi.org/10.1002/cem.1180080606>.
- [35] E. Bramanti, E. Benedetti, Determination of the secondary structure of isomeric forms of human serum albumin by a particular frequency deconvolution procedure applied to fourier transform IR analysis, *Biopolymers* 38 (1998) 639–653, [https://doi.org/10.1002/\(SICI\)1097-0282\(199605\)38:5<639::AID-BIP8>3.0.CO;2-T](https://doi.org/10.1002/(SICI)1097-0282(199605)38:5<639::AID-BIP8>3.0.CO;2-T).
- [36] Y.N. Chirgadze, O.V. Fedorov, N.P. Trushina, Estimation of amino acid residue side-chain absorption in the infrared spectra of protein solutions in heavy water, *Biopolymers* 14 (1975) 679–694, <https://doi.org/10.1002/bip.1975.360140402>.
- [37] H.J. Salavagione, J. Sherwood, M. De Bruyn, V.L. Budarin, G.J. Ellis, J.H. Clark, P. S. Shuttleworth, Identification of high performance solvents for the sustainable processing of graphene, *Green Chem.* 19 (2017) 2550–2560, <https://doi.org/10.1039/C7GC00112F>.
- [38] Z. Guo, H. Zhang, S. Lu, Z. Wang, S. Tang, J. Shao, Z. Sun, H. Xie, H. Wang, X.-F. Yu, P.K. Chu, From black phosphorus to phosphorene: basic solvent exfoliation, evolution of Raman scattering, and applications to ultrafast photonics, *Adv. Funct. Mater.* 25 (2015) 6996–7002, <https://doi.org/10.1002/adfm.201502902>.
- [39] A.H. Woomer, T.W. Farnsworth, J. Hu, R.A. Wells, C.L. Donley, S.C. Warren, Phosphorene: synthesis, scale-up, and quantitative optical spectroscopy, *ACS Nano* 9 (2015) 8869–8884, <https://doi.org/10.1021/acsnano.5b02599>.
- [40] Z. Torbatian, R. Asgari, Optical absorption properties of few-layer phosphorene, *Phys. Rev. B* 98 (2018) 205407, <https://doi.org/10.1103/PhysRevB.98.205407>.
- [41] X. Ge, Z. Xia, S. Guo, Recent advances on black phosphorus for biomedicine and biosensing, *Adv. Funct. Mater.* 29 (2019), <https://doi.org/10.1002/adfm.201900318>.
- [42] A.M. Ross, G.M. Paternò, S. Dal Conte, F. Scotognella, E. Cinquanta, Anisotropic complex refractive indices of atomically thin materials: determination of the optical constants of few-layer black phosphorus, *Materials* 13 (2020) 5736, <https://doi.org/10.3390/ma13245736>.
- [43] L. Zeng, X. Zhang, Y. Liu, X. Yang, J. Wang, Q. Liu, Q. Luo, C. Jing, X.-F. Yu, G. Qu, P.K. Chu, G. Jiang, Surface and interface control of black phosphorus, *Chem* 8 (2022) 632–662, <https://doi.org/10.1016/j.chempr.2021.11.022>.
- [44] J. Kang, J.D. Wood, S.A. Wells, J.-H. Lee, X. Liu, K.-S. Chen, M.C. Hersam, Solvent exfoliation of electronic-grade, two-dimensional black phosphorus, *ACS Nano* 9 (2015) 3596–3604, <https://doi.org/10.1021/acsnano.5b01143>.
- [45] J. Shen, Y. He, J. Wu, C. Gao, K. Keyshar, X. Zhang, Y. Yang, M. Ye, R. Vajtai, J. Lou, P.M. Ajayan, Liquid phase exfoliation of two-dimensional materials by directly probing and matching surface tension components, *Nano Lett.* 15 (2015) 5449–5454, <https://doi.org/10.1021/acs.nanolett.5b01842>.
- [46] A.E. Del Rio Castillo, V. Pellegrini, H. Sun, J. Buha, D.A. Dinh, E. Lago, A. Ansaldo, A. Capasso, L. Manna, F. Bonaccorso, Exfoliation of few-layer black phosphorus in low-boiling-point solvents and its application in Li-ion batteries, *Chem. Mater.* 30 (2018) 506–516, <https://doi.org/10.1021/acs.chemmater.7b04628>.
- [47] Q. Zhou, Q. Chen, Y. Tong, J. Wang, Light-induced ambient degradation of few-layer black phosphorus: mechanism and protection, *Angew. Chem. Int. Ed.* 55 (2016) 11437–11441, <https://doi.org/10.1002/anie.201605168>.
- [48] S. Walia, Y. Sabri, T. Ahmed, M.R. Field, R. Ramanathan, A. Arash, S.K. Bhargava, S. Sriram, M. Bhaskaran, V. Bansal, S. Balendhran, Defining the role of humidity in the ambient degradation of few-layer black phosphorus, *2d Mater.* 4 (2016) 015025, <https://doi.org/10.1088/2053-1583/4/1/015025>.
- [49] M. van Druenen, F. Davitt, T. Collins, C. Glynn, C. O'Dwyer, J.D. Holmes, G. Collins, Evaluating the surface chemistry of black phosphorus during ambient degradation, *Langmuir* 35 (2019) 2172–2178, <https://doi.org/10.1021/acs.langmuir.8b04190>.
- [50] Y. Zhao, H. Wang, H. Huang, Q. Xiao, Y. Xu, Z. Guo, H. Xie, J. Shao, Z. Sun, W. Han, X. Yu, P. Li, P.K. Chu, Surface coordination of black phosphorus for robust air and water stability, *Angew. Chem.* 128 (2016) 5087–5091, <https://doi.org/10.1002/ange.201512038>.
- [51] The Engineering ToolBox (2005). Oxygen - Solubility in Fresh and Sea Water vs. Temperature. [online] Available at: [https://www.engineeringtoolbox.com/oxygen-n-solubility-water-d\\_841.html](https://www.engineeringtoolbox.com/oxygen-n-solubility-water-d_841.html) (Accessed 20 September 2023), (n.d.).
- [52] E. Passaglia, F. Cicogna, F. Costantino, S. Coiai, S. Legnaioli, G. Lorenzetti, S. Borsacchi, M. Geppi, F. Telesio, S. Heun, A. Ienco, M. Serrano-Ruiz, M. Peruzzini, Polymer-based black phosphorus (bP) hybrid materials by in situ radical polymerization: an effective tool to exfoliate bP and stabilize bP nanoflakes, *Chem. Mater.* 30 (2018), <https://doi.org/10.1021/acs.chemmater.7b05298>.
- [53] H.-Q. Bao, R.-B. Li, H.-D. Xing, C. Qu, Q. Li, W. Qiu, Crystalline orientation identification of phosphorene using polarized Raman spectroscopy without analyzer, *Appl. Sci.* 9 (2019) 2198, <https://doi.org/10.3390/app9112198>.
- [54] M. Akhtar, G. Anderson, R. Zhao, A. Alruqi, J.E. Mroczkowska, G. Sumanasekera, J. B. Jasinski, Recent advances in synthesis, properties, and applications of phosphorene, *NPJ 2D Mater. Appl.* 1 (2017) 5, <https://doi.org/10.1038/s41699-017-0007-5>.
- [55] W. Zhai, Y. Chen, Y. Liu, Y. Ma, P. Vijayakumar, Y. Qin, Y. Qu, Z. Dai, Covalently bonded Ni sites in black phosphorene with electron redistribution for efficient metal-lightweighted water electrolysis, *Nanomicro Lett.* 16 (2024) 115, <https://doi.org/10.1007/s40820-024-01331-6>.

- [56] A. Impellizzeri, A.A. Vorfolomeeva, N.V. Surovtsev, A.V. Okotrub, C.P. Ewels, D. V. Rybkovskiy, Simulated Raman spectra of bulk and low-dimensional phosphorus allotropes, *PCCP* 23 (2021) 16611–16622, <https://doi.org/10.1039/D1CP02636D>.
- [57] A. Kundu, D. Tristant, N. Sheremetyeva, A. Yoshimura, A. Torres Dias, K.S. Hazra, V. Meunier, P. Puech, Reversible pressure-induced partial phase transition in few-layer black phosphorus, *Nano Lett.* 20 (2020) 5929–5935, <https://doi.org/10.1021/acs.nanolett.0c01784>.
- [58] W. Lu, H. Nan, J. Hong, Y. Chen, C. Zhu, Z. Liang, X. Ma, Z. Ni, C. Jin, Z. Zhang, Plasma-assisted fabrication of monolayer phosphorene and its Raman characterization, *Nano Res.* 7 (2014) 853–859, <https://doi.org/10.1007/s12274-014-0446-7>.
- [59] S. Jana, S. Mukherjee, A. Ghorai, S.B.N. Bhaktha, S.K. Ray, Negative thermal quenching and size-dependent optical characteristics of highly luminescent phosphorene nanocrystals, *Adv. Opt. Mater.* 8 (2020), <https://doi.org/10.1002/adom.202000180>.
- [60] D. Hanlon, C. Backes, E. Doherty, C.S. Cucinotta, N.C. Berner, C. Boland, K. Lee, A. Harvey, P. Lynch, Z. Gholamvand, S.F. Zhang, K.P. Wang, G. Moynihan, A. Pokle, Q.M. Ramasse, N. McEvoy, W.J. Blau, J. Wang, G. Abellan, F. Hauke, A. Hirsch, S. Sanvito, D.D. O'Regan, G.S. Duesberg, V. Nicolosi, J.N. Coleman, Liquid exfoliation of solvent-stabilized few-layer black phosphorus for applications beyond electronics, *Nat. Commun.* 6 (2015), <https://doi.org/10.1038/ncomms9563>.
- [61] L. Deng, L. Wan, N. Zhou, S. Tang, Y. Li, Anisotropy diffusion of water nanodroplets on phosphorene: effects of pre-compressive deformation and temperature, *Comput. Mater. Sci.* 178 (2020) 109623, <https://doi.org/10.1016/j.commatsci.2020.109623>.
- [62] Y. Huang, J. Qiao, K. He, S. Bliznakov, E. Sutter, X. Chen, D. Luo, F. Meng, D. Su, J. Decker, W. Ji, R.S. Ruoff, P. Sutter, Interaction of black phosphorus with oxygen and water, *Chem. Mater.* 28 (2016) 8330–8339, <https://doi.org/10.1021/acs.chemmater.6b03592>.
- [63] A. Ziletti, A. Carvalho, D.K. Campbell, D.F. Coker, A.H. Castro Neto, Oxygen defects in phosphorene, *Phys. Rev. Lett.* 114 (2015) 046801, <https://doi.org/10.1103/PhysRevLett.114.046801>.
- [64] F. Benini, N. Bassoli, P. Restuccia, M. Ferrario, M.C. Righi, Interaction of Water and Oxygen Molecules with Phosphorene: An Ab Initio Study, *Molecules* 28 (2023) 3570, <https://doi.org/10.3390/molecules28083570>.
- [65] H. Wang, X. Yang, W. Shao, S. Chen, J. Xie, X. Zhang, J. Wang, Y. Xie, Ultrathin black phosphorus nanosheets for efficient singlet oxygen generation, *J. Am. Chem. Soc.* 137 (2015) 11376–11382, <https://doi.org/10.1021/jacs.5b06025>.
- [66] K. Murotomi, A. Umeno, M. Shichiri, M. Tanito, Y. Yoshida, Significance of singlet oxygen molecule in pathologies, *Int. J. Mol. Sci.* 24 (2023) 2739, <https://doi.org/10.3390/ijms24032739>.
- [67] W.F. Wong, A.J. Melendez, Frontiers in research reviews: cutting-edge molecular approach to therapeutics – introduction, *Clin. Exp. Pharmacol. Physiol.* 33 (2006) 480–481, <https://doi.org/10.1111/j.1440-1681.2006.04395.x>.
- [68] T. Entradas, S. Waldron, M. Volk, The detection sensitivity of commonly used singlet oxygen probes in aqueous environments, *J. Photochem. Photobiol. B* 204 (2020) 111787, <https://doi.org/10.1016/j.jphotobiol.2020.111787>.
- [69] M. Pica, R. D'Amato, Chemistry of phosphorene: synthesis, functionalization and biomedical applications in an update review, *Inorganics (basel)* 8 (2020), <https://doi.org/10.3390/inorganics8040029>.
- [70] A. Battisti, A. Palumbo Piccionello, A. Sgarbossa, S. Vilasi, C. Ricci, F. Ghetti, F. Spinozzi, A. Marino Gammazza, V. Giacalone, A. Martorana, A. Lauria, C. Ferrero, D. Bulone, M.R. Mangione, P.L. San Biagio, M.G. Ortore, Curcumin-like compounds designed to modify amyloid beta peptide aggregation patterns, *RSC Adv.* 7 (2017) 31714–31724, <https://doi.org/10.1039/C7RA05300B>.
- [71] A. Sgarbossa, D. Buselli, F. Lenci, In vitro perturbation of aggregation processes in  $\beta$ -amyloid peptides: a spectroscopic study, *FEBS Lett.* 582 (2008) 3288–3292, <https://doi.org/10.1016/j.febslet.2008.08.039>.
- [72] M. Biancalana, S. Koide, Molecular mechanism of Thioflavin-T binding to amyloid fibrils, *Biochim. Biophys. Acta* 1804 (2010) 1405–1412, <https://doi.org/10.1016/j.bbapap.2010.04.001>.
- [73] X. Chen, W. He, Y. Liang, C. Yuan, S. Zhang, F. Liu, Y. Xiao, Enhanced degradation of few-layer black phosphorus by fulvic acid: processes and mechanisms, *Water Res.* 238 (2023) 120014, <https://doi.org/10.1016/j.watres.2023.120014>.
- [74] S.D.P.L.H. Weiss M, Insulin Biosynthesis, Secretion, Structure, and Structure-Activity Relationships. [Updated 2014 Feb 1], in: Feingold KR, Anawalt B, Blackman MR, et al., Editors. Endotext [Internet]. South Dartmouth (MA): MDText. Com, Inc.; 2000-. Available from: <https://www.Ncbi.Nlm.Nih.Gov/Books/NBK279029/>, n.d.
- [75] N.A. Nevskaya, Y.N. Chirgadze, Infrared spectra and resonance interactions of amide-I and II vibrations of  $\alpha$ -helix, *Biopolymers* 15 (1976) 637–648, <https://doi.org/10.1002/bip.1976.360150404>.
- [76] H. Torii, M. Tasumi, Model calculations on the amide-I infrared bands of globular proteins, *J. Chem. Phys.* 96 (1992) 3379–3387, <https://doi.org/10.1063/1.461939>.
- [77] A. Barth, Infrared spectroscopy of proteins, *Biochim. Biophys. Acta* 1767 (2007) 1073–1101, <https://doi.org/10.1016/j.bbabi.2007.06.004>.
- [78] K.-Y. Chiang, F. Matsumura, C.-C. Yu, D. Qi, Y. Nagata, M. Bonn, K. Meister, True origin of amide I shifts observed in protein spectra obtained with sum frequency generation spectroscopy, *J. Phys. Chem. Lett.* 14 (2023) 4949–4954, <https://doi.org/10.1021/acs.jpcclett.3c00391>.
- [79] P.R. Shorten, C.D. McMahon, T.K. Soboleva, Insulin transport within skeletal muscle transverse tubule networks, *Biophys. J.* 93 (2007) 3001–3007, <https://doi.org/10.1529/biophysj.107.107888>.
- [80] E. Passaglia, F. Cicogna, G. Lorenzetti, S. Legnaioli, M. Caporali, M. Serrano-Ruiz, A. Ienco, M. Peruzzini, Novel polystyrene-based nanocomposites by phosphorene dispersion, *RSC Adv.* 6 (2016), <https://doi.org/10.1039/c6ra10133j>.